Imperial College London

Temperature dependance of the global ocean biological carbon sink

Author: Junyue Zhang

Date: 25/08/2022

Word count of the main text: 5824

Supervisor: Dr Emma Cavan

Co-supervisor: Prof Stephanie Henson

CID: 02125178

Department of Life Sciences

A thesis submitted in partial fulfilment of the requirements for the degree of Master of Science at Imperial College London

Submitted for the MSc in Computational Methods in Ecology and Evolution

Declaration

The data were collected and assembled from published papers and public websites.

I am responsible for data processing and cleaning.

Two mathematical models were developed by me.

My supervisor gave me detailed suggestions and patient guidance during this project.

Contents

Abstract

This thesis aims to use sea surface temperature (SST) and net primary production (NPP) to investigate whether sinking and remineralization rates of particulate organic carbon (POC) are sufficient to explain the attenuation of POC in the global ocean. POC sinking and remineralization rates and relevant information were collected from published papers, and linear models were fitted to the compiled data, followed by estimating the remineralization length scale (RLS) based on the functions derived from linear regressions using sea temperatures and NPP as inputs. A significant difference between the modelled RLS and observations was observed, suggesting that the POC sinking rate and remineralization rate are not sufficient to explain the attenuation of POC in the water column. However, median values of the modelled RLS and observations were quite similar, mean values were close, the modelled RLS was on the right order of magnitude, and the discrepancy was only due to different distributions of values. Therefore, global mapping projections were performed to bring the functions that use temperature and NPP to predict the POC sinking rate and remineralization rate into global biogeochemical models. The global map of transfer efficiency through the mesopelagic zone shows high values in tropical and subtropical regions and low values at high latitudes, with a mean of 0.13, indicating that globally an average of 13% of POC exported from the euphotic zone survives the remineralization to reach 1000 m depth. The mesopelagic transfer efficiency ranges between 0.012 and 0.66, which is very close to previous studies. Overall, this study contributes to the understanding of the attenuation of POC and mesopelagic particle transfer efficiency.

1 Introduction

The biological carbon pump (BCP) is one of the most important regulators of vertical carbon distribution in the ocean and, therefore, of the CO_2 surface partial pressure that controls the air-sea CO_2 exchange (Bishop, 2009). It mainly consists of phytoplankton, zooplankton, and bacteria that decompose the detritus. The first part of the BCP is that phytoplankton produce organic matter, which feeds zooplankton and may become detritus. Decomposing detritus decreases the partial pressure of CO_2 at the surface, while the production of organic carbon and its sinking increases the partial pressure. The biological pump is vital to the global carbon cycle since it transports carbon from the atmosphere to the deep ocean, and the carbon is stored in the deep ocean for centuries (Chisholm,1995). Without the biological pump, which delivers around 11 GtC yr^{-1} to the ocean interior, atmospheric CO_2 levels would be about 200 ppm higher than at present (Sanders et al., 2014; Boyd, 2015; Barange et al., 2017).

The first stage in the biological pump is primary production. The CO_2 dissolved from the atmosphere to the ocean surface is converted through photosynthesis by phytoplankton into particulate organic carbon (POC) in the euphotic zone. Krill and small zooplankton grazers consume phytoplankton and are subsequently preyed upon by higher trophic levels (Cavan et al., 2019). Microbes, zooplankton, and their consumers transform POC into fecal pellets, organic aggregates, carcasses, and other forms. These are then transported to the ocean interior via sinking and diel vertical migration by zooplankton and fish (Turner, 2015). In the water column, a proportion of POC is converted back to CO_2 by heterotrophic microorganisms and zooplankton, resulting in the vertical gradient in dissolved inorganic carbon (DIC) concentration. Between 1% and 40% of primary production is exported out of the euphotic zone and then decreases dramatically towards the bottom of the mesopelagic zone. Only around 1% of the organic carbon formed at the ocean surface reaches the seafloor (Basu and Mackey, 2018; Passow and Carlson, 2012; Turner, 2015).

Since the export of POC mostly determines the overall efficiency of the biological pump (Kim et al., 2011), only the gravitational settling of POC was investigated in this project. Martin et al. (1987) proposed a power-law expression to predict POC flux in the deep ocean as listed below (Eq. 1):

$$f_z = f_{z0}(z/z_0)^{-b} \qquad [1]$$

in which f_z is the POC flux at depth z, z_0 is the reference depth corresponding to the export flux f_{z0} at the surface layer, and the coefficient b describes the attenuation of POC flux with depth. Martin et al. (1987) calculated a composite b value of 0.858 $\pm$ 0.1 for the open ocean from POC flux measurements at several eastern North Pacific locations. This power-law expression has been widely used, especially in the Ocean Carbon Model Intercomparison Project II runs (Boyd and Trull, 2007).

However, the power-law equation (Eq. 1) is sensitive to the reference depth, and an alternative exponential equation was advocated to describe the attenuation of POC flux with depth in the upper ocean as listed below (Eq. 2) (Boyd and Trull, 2007):

$$f_z = f_{z_0}\exp\left(-(z - z_0)/z^*\right) \qquad [2]$$

in which z^* is the remineralization length scale (RLS) for the POC flux decay with depth. z^* indicates the depth at which 63% of the POC flux had been remineralized, that is, respired back to CO_2 in the water column, primarily by zooplankton and heterotrophic microbes. The following equation was used to calculate the estimated z^* for microbial remineralization (Eq. 3) (Cavan et al., 2017):

$$z^* = w/k \qquad [3]$$

in which w is the average POC sinking velocity and k is the microbial carbon-specific remineralization rate.

The efficiency of the biological pump is primarily determined by aggregate sinking velocities and degradation rates of the organic matter within the settling aggregates. The export of organic carbon is high when sinking velocities are high and/or degradation rates are low (Iversen & Ploug, 2013). According to Siegel et al. (1990),

the nature of the particle has a significant impact on the sinking rate. For instance, ultraplankton sink at <0.1–2 m d^{-1} (Bienfang, 1980), algal aggregates sink at 40–150 m d^{-1} (Smetacek, 1985), and fecal pellets of mesozooplankton sink at 20–900 m d^{-1} (Fowler and Small, 1972). Helmke et al. (2005) calculated a mean particle velocity of 75 m d^{-1} with absolute values between 59 and 170 m d^{-1} at 3580 m depth in the NW African upwelling area. Fischer and Karakaş (2009) compiled a table for sinking rates of particles in the Atlantic Ocean based on the seasonal flux data using the major peak and the correlation method. They proposed that the sinking rate of particles determined from sediment trap samples ranged between 73 and 741 m d^{-1}. Alonso-González et al. (2010) suggested that globally, slow-sinking particles (0.7–11 m d^{-1}) account for ~60% of the export flux, while fast-sinking particles (>326 m d^{-1}) account for ~25% of the export flux.

For the remineralization of POC, Ploug and Grossart (2000) directly measured bacterial growth, respiration, and POC on individually cultured diatom aggregates of different sizes. They suggested that the POC-specific respiration rate on aggregates was 0.083 d^{-1} at 16 °C, and 40% of the initial POC content was respired after six days. Bidle et al. (2002) measured POC-specific remineralization rates on diatom detritus ranging from 0.09 to 0.28 d^{-1} using a natural bacterial assemblage from temperate Pacific waters. Iversen and Ploug (2010) measured an average carbon-specific respiration rate of 0.13 d^{-1} for lab-formed aggregates of three different phytoplankton cultures at 15 °C, with a range of 0.005–0.422 d^{-1}. Similarly, Iversen et al. (2010) measured an average carbon-specific respiration rate of 0.13 d^{-1} for aggregates formed in roller tanks from peak fluorescence waters off Cape Blanc, Africa at 18 °C, with a range of 0.02–0.36 d^{-1}. Iversen and Ploug (2013) observed no direct influence of temperature on aggregate sinking velocity. The average carbon-specific respiration rate during the experiment was 0.12 ± 0.03 at 15 °C and decreased 3.5-fold when the temperature was lowered to 4 °C.

However, few studies have used environmental variables such as temperature and net primary production (NPP) to estimate the efficiency of organic carbon transfer from the surface to the deep ocean. The remineralization length scale is not well parameterized in ocean biogeochemical models. This thesis aims to use sea surface temperature and net primary production to investigate whether the POC sinking rate and remineralization rate are sufficient to explain the attenuation of POC in the global ocean. The hypothesis is that the remineralization length scales estimated using POC sinking rates and remineralization rates approximate the observations derived from POC flux attenuation profiles. This study first used temperature and NPP to predict the POC sinking rate and remineralization rate and then compared the modelled RLS with observations, followed by predicting the particle transfer efficiency through the mesopelagic zone. This study contributes to a clearer understanding of the attenuation of POC and mesopelagic transfer efficiency.

2 Methods

2.1 Data collection

To begin with, a global dataset compiled by Mouw et al. (2016) was used to acquire observed remineralization length scales. Mouw et al. (2016) reported that this global ocean flux rates dataset is the most comprehensive compilation of POC flux around the world. This compiled dataset comprises a total of 15792 individual POC flux estimates at 673 unique sites from sediment traps and ^{234}Th between 1976 and 2012. The researchers focused on collecting short-term sediment trap deployments, with a median deployment interval of 14 days. 93% of qualified measurements were deployed in 20 days or less, and 59% were deployed in 14 days or less (Mouw et al., 2016). Data can be accessed from PANGAEA, https://doi.org/10.1594/PANGAEA.855594. The entire dataset was imported into R, and data were arranged in columns of reference, latitude, longitude, deployed time, retrieved time, depth of sediment trap deployment, flux of particulate organic carbon, *etc*. Rows with missing POC flux were deleted since this project aims to investigate the sedimentation of POC in the water column.

World Ocean Atlas data were used to collect sea surface temperatures at different depths. WOA 2018 data contain annual, seasonal, and monthly statistical mean of ocean temperature on the 1° grid from 1955 to 2017 (Locarnini et al., 2018). WOA 2018 data can be accessed from National Centers for Environmental Information, https://www.ncei.noaa.gov/access/world-ocean-atlas-2018/. Each data file in WOA 2018 is arranged in columns of latitude, longitude, and temperatures at different depths. Ocean net primary production (NPP) data were accessed from Ocean Productivity, http://sites.science.oregonstate.edu/ocean.productivity/standard.product.php. The NPP data are based on the standard Vertically Generalized Production Model (VGPM) algorithm (Behrenfeld & Falkowski, 1997a). Monthly XYZ files with the grid size of 1080 by 2160 from MODIS R2018 Data were selected and imported into R. Each file has

three columns: latitude, longitude, and NPP value. An NPP value of -9999 means that no data is available. Therefore, rows with no data were removed. As this study focuses on climatological seasonal variations, years of temperature and NPP data were disregarded.

To predict the POC sinking rate using temperature and NPP, a table for POC sinking rates was developed based on the dataset created by BB Cael et al. (2021). They arranged the dataset in columns of equivalent spherical diameter, sinking velocity, and reference. For the same reference, there is a series of equivalent spherical diameters and corresponding sinking velocities with the same particle type, method of measurement, and source of collection. The median of sinking velocities was used to represent the sinking rate for each reference since the median is the most accurate indicator of central tendency and is unaffected by extreme outliers or asymmetric distributions. Additional parameters were obtained by searching the papers cited by BB Cael et al. (2021). The table for the POC sinking rate can be found in Table 1 in Supplementary Material, arranged in columns of citation, particle type, latitude, longitude, method, measured time, sinking velocity, *etc*. Subsequently, a table for POC remineralization rates was compiled by reviewing published papers, as shown in Table 2 in Supplementary Material, arranged in columns of reference, latitude, longitude, measured time, remineralization rate, *etc*.

2.2 Obtaining observed and modelled remineralization length scales

In the global ocean flux rates dataset (Mouw et al., 2016), there are more than two POC flux measurements for 25.6% of locations and times, corresponding to different depths from shallow to deep. The exponential equation (Eq. 2) above can be used to extract the observed RLS from the slope coefficient as listed below (Eq. 4):

$$z = -z^* \times log_e(f_z) + z^* \times log_e(f_{z_0}) + z_0 \quad [4]$$

in which z is the depth, f_z is the flux at depth z, and z^* is the remineralization length scale. As only one or two POC flux measurements were available for 74.4% of the

locations and times, the corresponding data were discarded in the linear regression. The observed remineralization length scales were obtained from the negative slope coefficients in POC flux attenuation profiles. 23% of the profiles showed negative RLS and these were removed as they were physically unrealistic.

NPP values were acquired from climatological means of Standard VGPM data according to the month of measurement and the closest location to the measurement site. Similarly, sea surface temperatures were acquired from climatological means of WOA 2018 data according to the month of measurement, the closest location to the measurement site, and the closest depth to the collection depth. After compiling the temperature and NPP values into tables, multiple linear regressions were carried out to estimate the POC sinking rate and remineralization rate. By comparing p-values, R^2 and AIC values, the models with the best goodness of fit were selected for the POC sinking rate and remineralization rate, respectively. In the global ocean flux rates dataset (Mouw et al., 2016), functions derived from the linear models were applied to estimate POC sinking rates and remineralization rates using sea surface temperatures and NPP values as inputs. The modelled remineralization length scales were obtained by dividing the POC sinking rates by remineralization rates and then compared to the observations. Since this study focuses on the attenuation of POC in the mesopelagic zone, data with depths less than 100 m or greater than 2000 m were discarded. The Wilcoxon test was performed in R to observe the difference between the modelled RLS and observations, followed by investigating the residuals in terms of temperature and NPP.

2.3 Global mapping

Global POC sinking rates and remineralization rates were estimated based on the functions derived from linear regressions using NPP values from Standard VGPM data and annual statistical means of sea surface temperatures at 100 m depth from WOA

2018 data as inputs. Global remineralization length scales were then obtained by dividing global POC sinking rates by remineralization rates. The global particle export efficiency, defined as the POC flux at 100 m divided by primary production (Henson et al., 2012), was estimated using the sea surface temperature at 100 m, based on the relationship between the POC export efficiency and temperature produced by Henson et al. (2011) (Eq. 5):

$$E - ratio = 0.23e^{(-0.08 \times SST)} \quad [5]$$

in which SST is the sea surface temperature and $E - ratio$ is the particle export efficiency. The POC fluxes at 100 m were estimated by multiplying the particle export efficiencies with NPP values. The global POC fluxes in the deep ocean were estimated using Eq. 2, with the POC fluxes at 100 m as the shallow reference fluxes. The global particle transfer efficiencies through the mesopelagic zone were estimated by dividing POC fluxes at 1000 m by POC fluxes at 100 m (Francois et al., 2002).

3 Results

3.1 POC sinking and remineralization rates

To estimate the POC sinking rate, several models were fitted to the data for the POC sinking rate, temperature, and NPP in Table 1 in Supplementary Material. An exponential function (Eq. 6) was chosen as the goodness of fit was the best (R^2 = 0.57, p < 0.01):

$$w = 3.867exp^{(0.139\times SST+0.00045\times NPP)} \qquad [6]$$

in which w is the POC sinking rate, SST is the sea surface temperature, and NPP is the net primary production. As the POC remineralization rate (k) was highly linearly correlated with temperature and less correlated with NPP, a linear function (Eq. 7) was selected to estimate the POC remineralization rate using temperature data as input, as shown in Table 2 in Supplementary Material (R^2 = 0.98, p < 0.001):

$$k = 0.00756 + 0.00653 \times SST \qquad [7]$$

in which k indicates the POC remineralization rate. The modelled RLS was then estimated by dividing the POC sinking rate derived from Eq. 6 by the remineralization rate derived from Eq. 7. The observed RLS had a mean of 688.6 m, while the modelled RLS had a mean of 518.3 m. Figure 1 shows a boxplot for observed and modelled RLS.

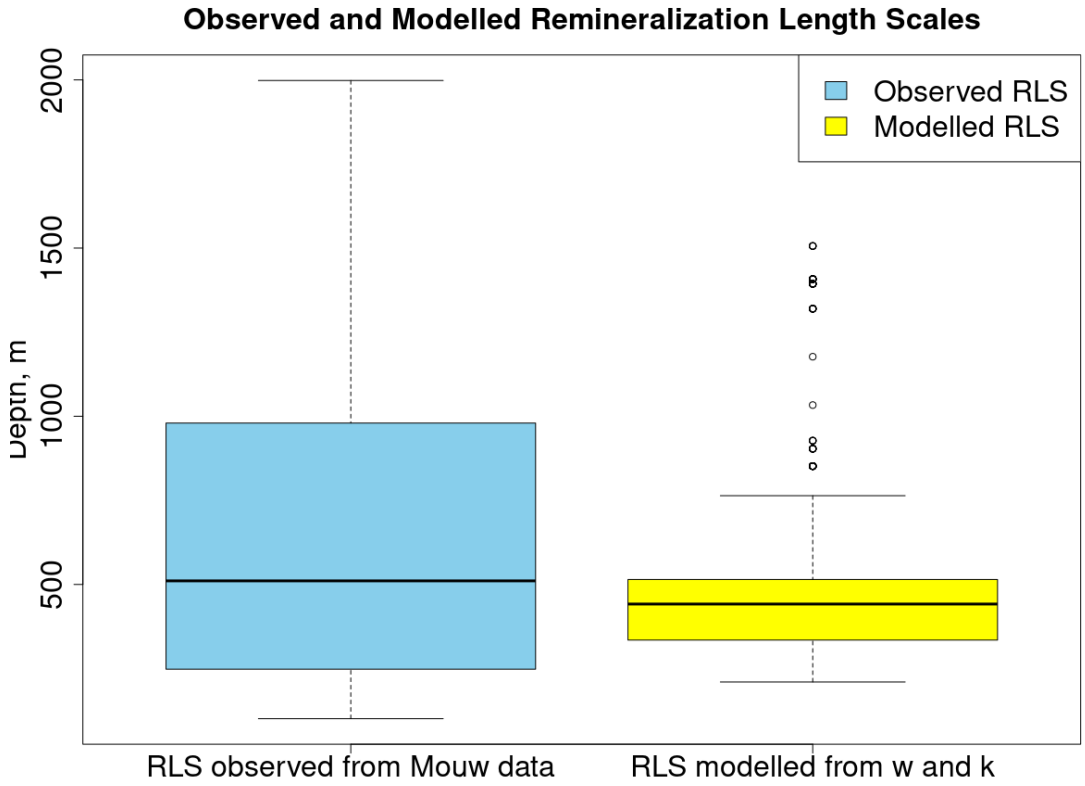

Figure 1 – Boxplot for observed and modelled remineralization length scales. The left one is the RLS observed from the POC flux attenuation profiles in the global ocean flux rates dataset compiled by Mouw et al. (2016). The right one is the RLS modelled from *w* and *k* using sea surface temperatures from WOA 2018 data and net primary production from Standard VGPM data as inputs. The modelled values are at the same locations as the observations. The black line in the box indicates the median and the lower and upper edges of the box indicate the 25th and 75th percentiles, respectively. The points outside the box indicate potential outliers.

As shown in Figure 1, the observed remineralization length scale had a wider range (100.9–1998.2 m) than the modelled RLS (210–1931.1 m), and the observed RLS was generally higher than the modelled RLS. The 25th and 75th percentiles of the modelled RLS were 335.4 m and 514.6 m, respectively, with a median of 441.8 m. The 25th and 75th percentiles of observations were 248.4 m and 979.3 m, respectively, with a median of 510.7 m. As neither the observed RLS nor the modelled RLS followed a normal

distribution, a non-parametric Wilcoxon test was performed to test the hypothesis that the modelled RLS derived from the POC sinking rate and remineralization rate approximates the observation derived from the POC flux attenuation profile. The p-value was less than 0.001, indicating that at the 0.1% significance level, there was a significant difference between the observed RLS and modelled RLS. Therefore, this contradicts the initial hypothesis that modelled RLS would be close to the observation and, in fact, suggests that the POC sinking rate and remineralization rate are not sufficient to explain the attenuation of POC in the water column. To investigate residuals between the observed RLS and modelled RLS, Figures 2 and 3 present the variations of the residuals with temperature and NPP, respectively.

3.2 Residuals

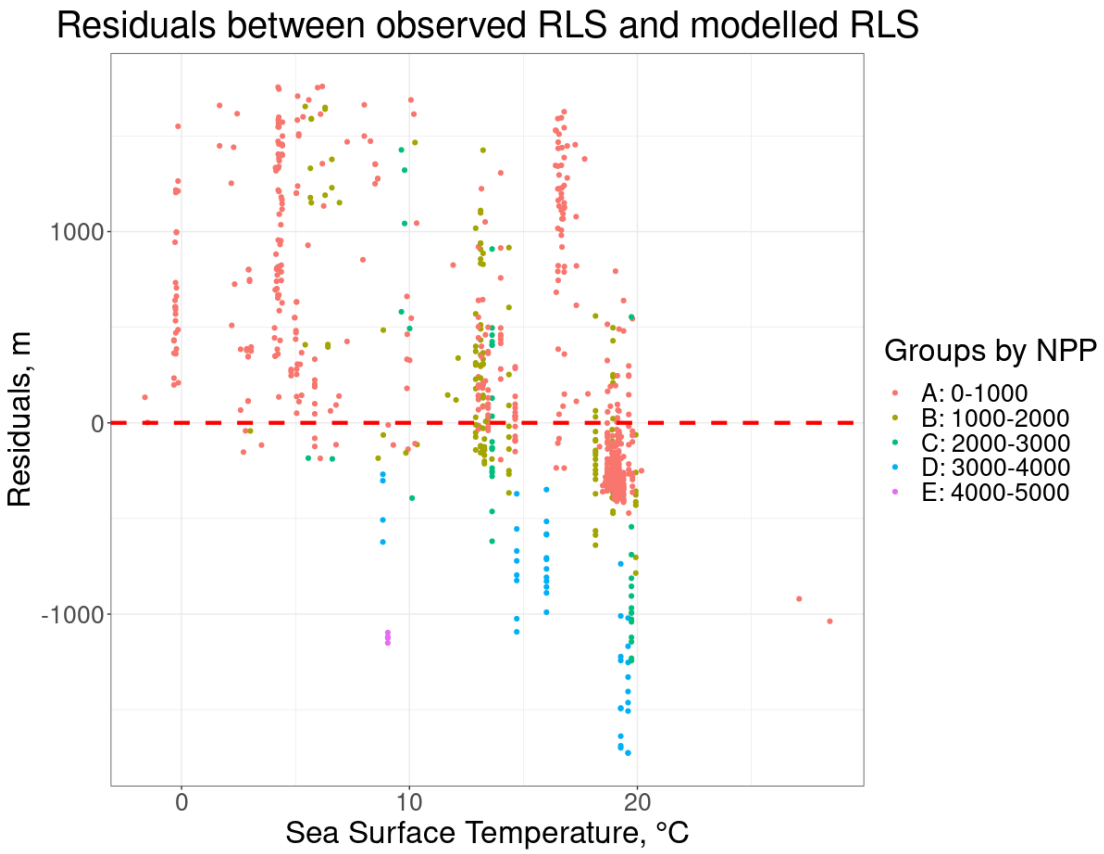

Figure 2 – Variation of the residuals with sea surface temperature. The colors of the data points were grouped by net primary production (mgC m^{-2} d^{-1}).

As shown in Figure 2, 73% of the data points were between 10 and 20 °C, and 65% had residuals between -500 and 500 m. When the sea surface temperature was less than 15 °C, 78.53% of data points had positive residuals, indicating that the observations were mainly larger than the modelled values. However, when the temperature was greater than 15 °C, 78.74% of data points had negative residuals, indicating that the observations were mainly less than the modelled values. It can be observed that 78.59% of the data points between 15 and 20 °C were clustered with negative residuals.

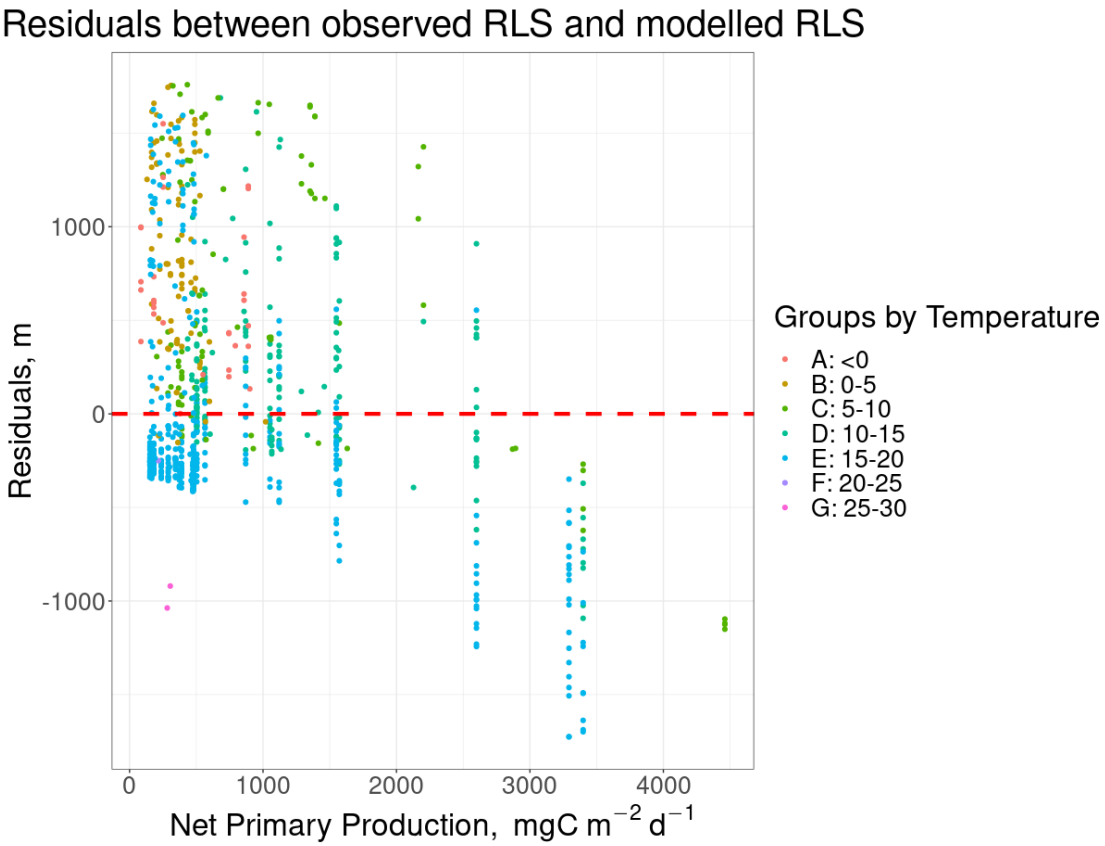

Figure 3 – Variation of the residuals with net primary production. The colors of the data points were grouped by sea surface temperature (°C).

It can be seen in Figure 3 that 72% of the global data points were clustered below 1,000 mgC m^{-2} d^{-1} of net primary production. When the NPP was greater than 2,000 mgC m^{-2} d^{-1}, 84% of data points had negative residuals, indicating that the observations

were predominantly lower than the modelled values. However, when NPP was below 2,000 mgC m^{-2} d^{-1}, 47% of the data points had negative residuals, while 53% had positive residuals. This indicates that nearly half of the observations were lower than the modelled RLS, while the other half were higher than the modelled values. Although the modelled RLS was significantly different from the observation, the medians were quite similar, the means were close, and the modelled RLS was on the right order of magnitude, only the distributions of values were different. Therefore, global mapping projections were subsequently carried out to bring Eq.6 and Eq.7 into global biogeochemical models and to test the hypothesis that there is a distinct geographical pattern in the particle transfer efficiency across the global ocean. Figures 4–11 demonstrate global patterns in NPP, annual sea surface temperature at 100 m, remineralization length scale, particle export efficiency, POC flux at 100 m, POC flux at 1000 m, POC flux at 2000 m, and particle transfer efficiency, respectively.

3.3 Global maps

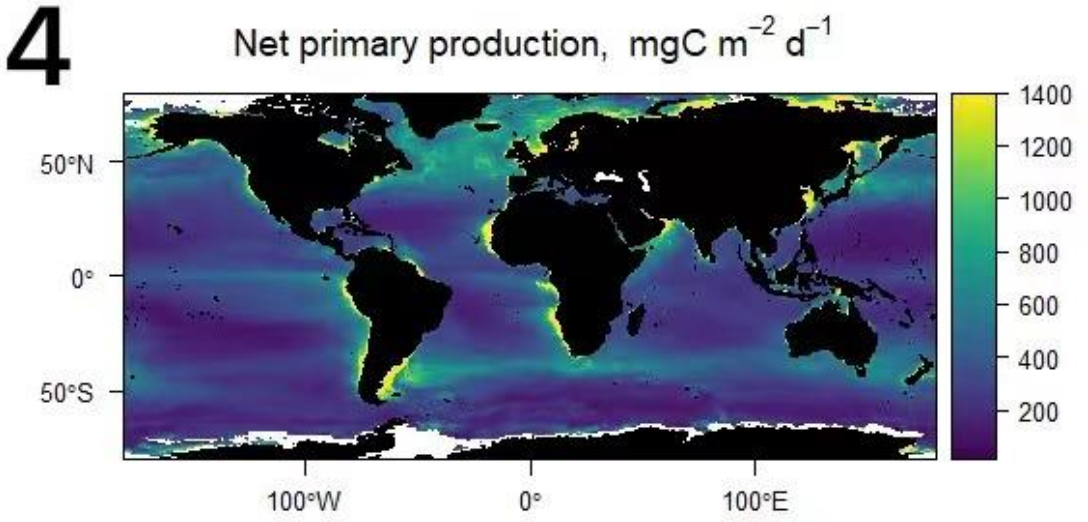

5

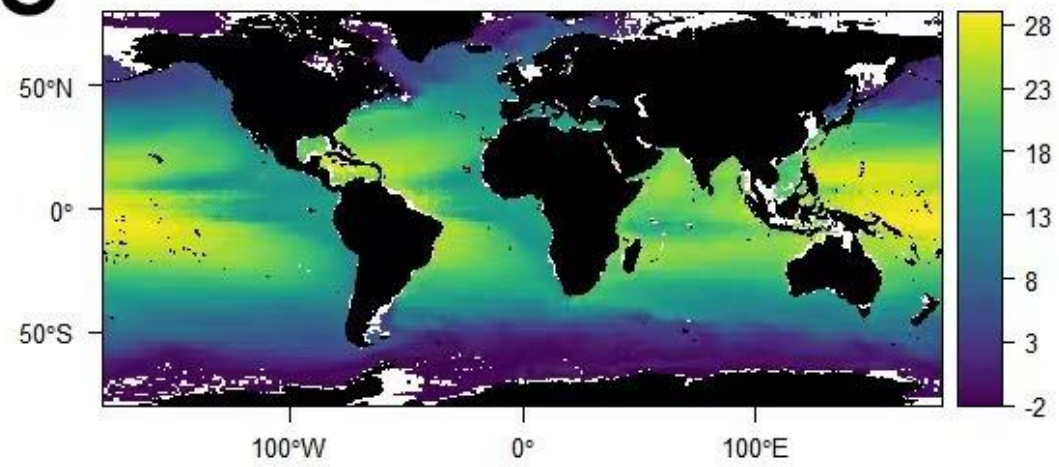
Sea Surface Temperature at 100 m depth, °C
50°N
0°
50°S
100°W
0°
100°E
28
23
18
13
8
3
-2

6

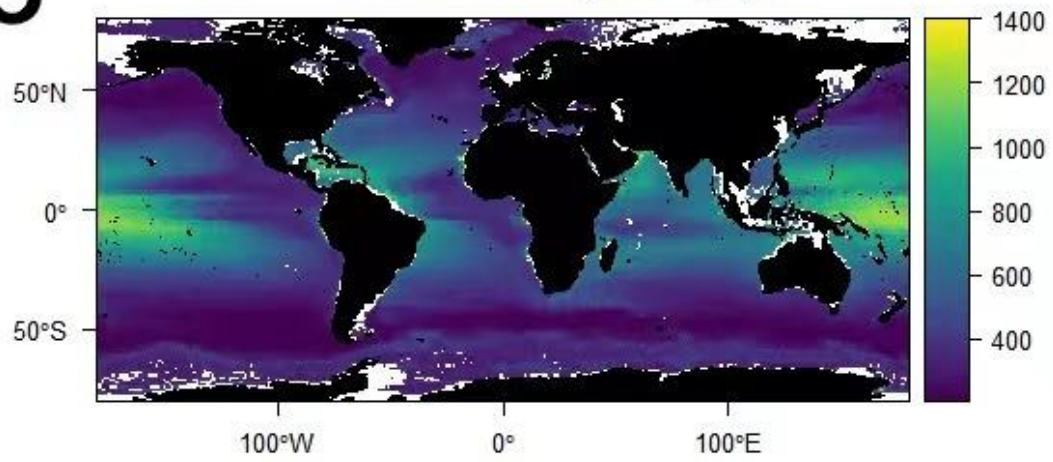
Remineralization length scale, m
50°N
0°
50°S
100°W
0°
100°E
1400
1200
1000
800
600
400

7

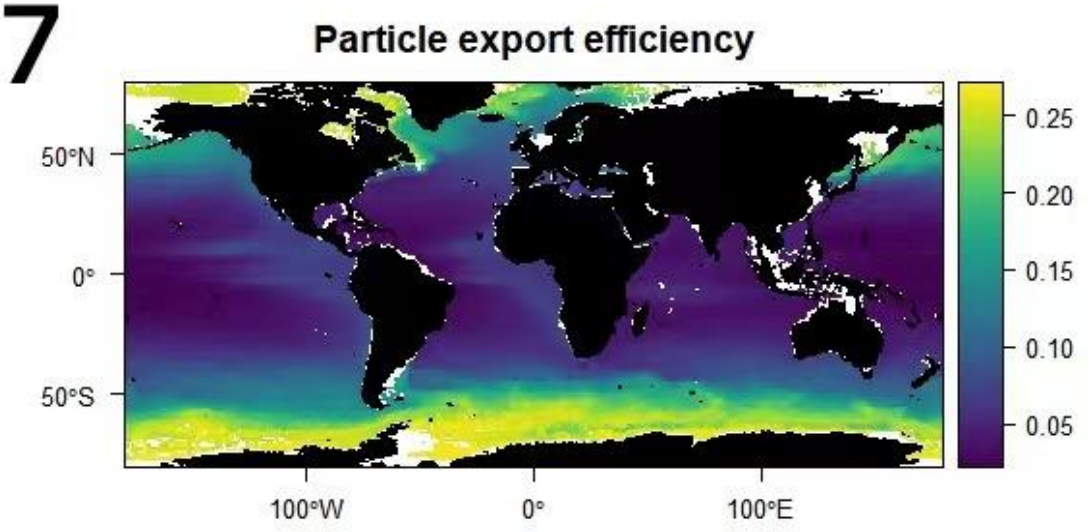
Particle export efficiency
50°N
0°
50°S
100°W
0°
100°E
0.25
0.20
0.15
0.10
0.05

8

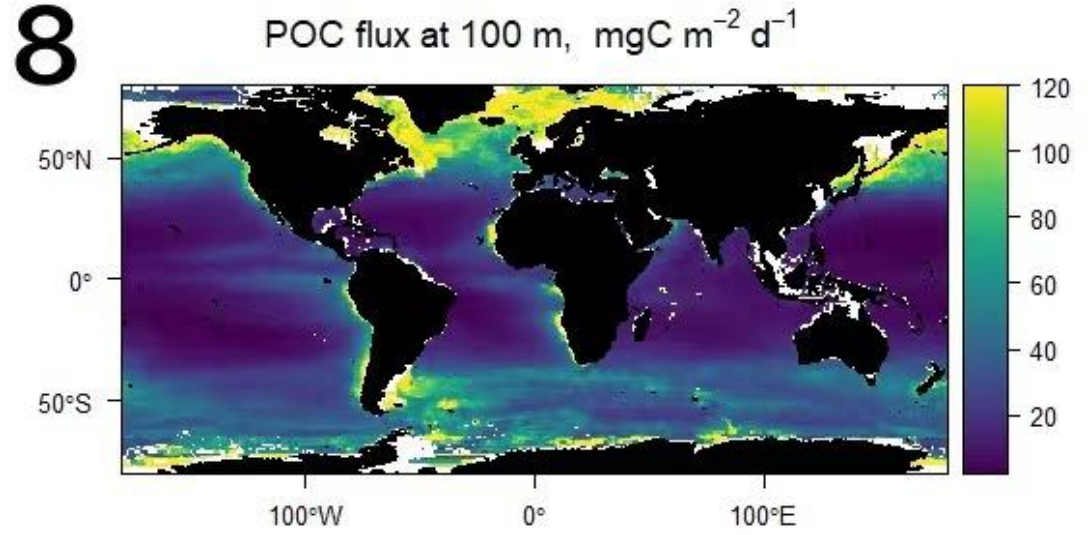
POC flux at 100 m, mgC m^{-2} d^{-1}
50°N
0°
50°S
100°W
0°
100°E
120
100
80
60
40
20

9

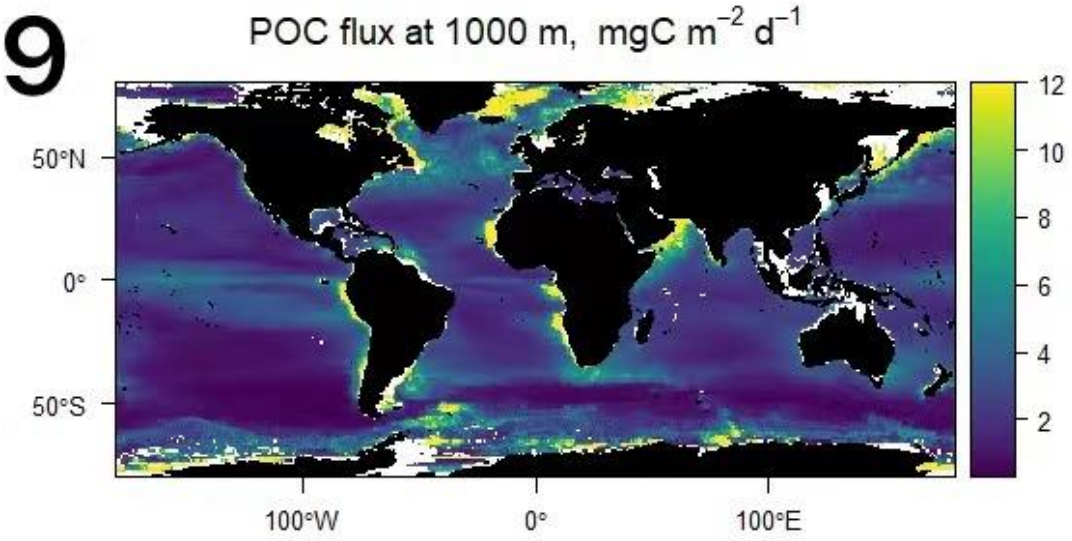
POC flux at 1000 m, mgC m^{-2} d^{-1}
50°N
0°
50°S
100°W
0°
100°E
12
10
8
6
4
2

10

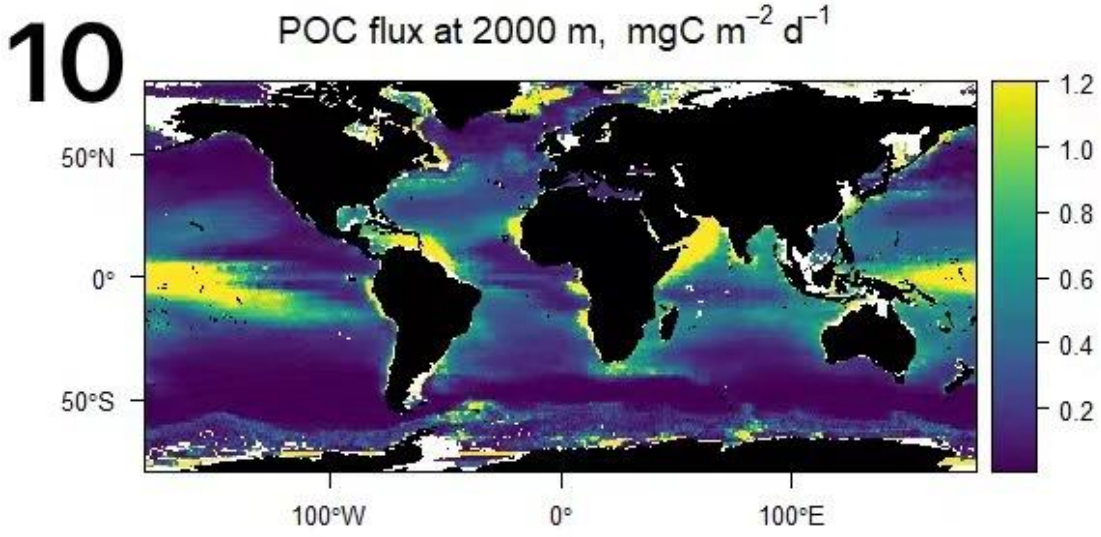
POC flux at 2000 m, mgC m^{-2} d^{-1}
50°N
0°
50°S
100°W
0°
100°E
1.2
1.0
0.8
0.6
0.4
0.2

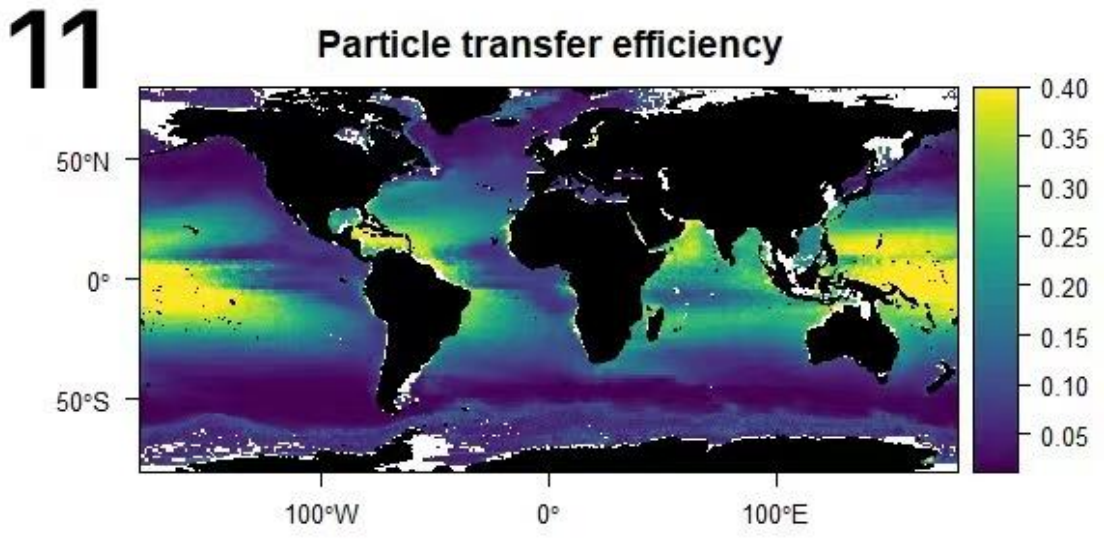

Figure 4 – Global map of satellite-derived net primary production based on the climatological mean of Standard VGPM data. Figure 5 – Global map of annual sea surface temperature at 100 m depth based on the climatological mean of WOA 2018 data. Figure 6 – Global map of remineralization length scale estimated by dividing the POC sinking rates derived from Eq. 6 by remineralization rates derived from Eq. 7, using sea surface temperatures from WOA 2018 data and NPP from Standard VGPM data as inputs. Figure 7 – Global map of particle export efficiency estimated using sea surface temperatures at 100 m from WOA 2018 data as inputs based on the relationship between the POC export efficiency and temperature produced by Henson et al. (2011) (Eq. 5). Figure 8 – Global map of POC flux at 100 m estimated by multiplying the particle export efficiency with NPP from Standard VGPM data. Figure 9 – Global map of POC flux at 1000 m estimated using Eq. 2, with the POC flux at 100 m as the shallow reference flux. Figure 10 – Global map of POC flux at 2000 m estimated using Eq. 2, with the POC flux at 100 m as the shallow reference flux. Figure 11 – Global map of particle transfer efficiency estimated by dividing the POC flux at 1000 m by the POC flux at 100 m (Francois et al., 2002).

As shown in Figure 4, the global map of NPP shows high values (>1,000 mgC m^{-2} d^{-1}) around the coasts of the continents and in the middle and high latitudes of the Northern

Hemisphere. In the Southern Ocean, NPP was mostly moderate (~400 mgC m^{-2} d^{-1}), with higher values downstream of continents and islands. With slightly higher values in equatorial upwelling regions, NPP was generally low (<200 mgC m^{-2} d^{-1}) at low latitudes. The 25th percentile, median, and 75th percentile of net primary production across the global ocean were 225.42, 318.47, and 505.61 mgC m^{-2} d^{-1}, respectively, with a mean of 457.01 mgC m^{-2} d^{-1}.

As can be seen in Figure 5, annual sea surface temperatures at 100 m were relatively high at low and middle latitudes, reaching around 20 °C, and especially high in the equatorial regions, approaching 30 °C. High latitude regions, such as the Southern Ocean and the subarctic oceans, were very cold, with annual temperatures below zero. This suggests that there is a large difference of more than 20 °C in the annual temperature between low and high latitudes across the global ocean.

The global map of RLS (Figure 6) shows high values (>1,000 m) at low latitudes, especially in the equatorial Pacific, the Indian Ocean, and Atlantic coastal areas, which indicates that organic particle flux decreases by 63% below 1000 m depth. Intermediate values of RLS (~400–600 m) occurred at the mid-latitudes, and low values (<200 m) occurred at high latitudes, such as the Southern Ocean and the subarctic oceans. The 25th percentile, median, and 75th percentile of RLS across the global ocean were 309.6, 377.6, and 552.3 m, respectively, with a mean of 453.4 m, indicating that on average, 63% of the POC flux had been remineralized at a depth of 453.4 m globally.

The global map of particle export efficiency (Figure 7) shows high values (>0.25) in the Southern Ocean and Northern Hemisphere high latitudes, which indicates that more than 25% of net primary production is exported below the euphotic zone. Particulate export efficiencies were intermediate (~0.10–0.15) at mid-latitudes and slightly higher in some coastal areas. Low values (<0.05) occurred at low latitudes, such as in

equatorial upwelling regions where NPP values are slightly higher than in neighboring areas. The 25th percentile, median, and 75th percentile of particulate export efficiency across the global ocean were 0.044, 0.076, and 0.19, respectively, with a mean of 0.11, indicating that on average, 11% of net primary production is exported out of the euphotic zone globally.

The global maps of POC flux at 100 m (Figure 8) and 1000 m (Figure 9) show a similar geographical pattern. High values of POC flux (Figure 8: >100 mgC m^{-2} d^{-1}; Figure 9: >10 mgC m^{-2} d^{-1}) were found at high latitudes and around the coasts of the continents. Intermediate values (Figure 8: ~40–60 mgC m^{-2} d^{-1}; Figure 9: ~4–6 mgC m^{-2} d^{-1}) occurred at mid-latitudes and were higher in coastal regions and downstream of continental landmasses and islands. Low values (Figure 8: <20 mgC m^{-2} d^{-1}; Figure 9: <2 mgC m^{-2} d^{-1}) were observed at low latitudes and were slightly higher in equatorial upwelling regions. The 25th percentile, median, and 75th percentile of the POC flux at 100 m across the global ocean were 12.39, 30.75, and 54.24 mgC m^{-2} d^{-1}, respectively, with a mean of 44.72 mgC m^{-2} d^{-1}. And the 25th percentile, median, and 75th percentile of the POC flux at 1000 m were 1.56, 2.47, and 3.97 mgC m^{-2} d^{-1}, respectively, with a mean of 4.43 mgC m^{-2} d^{-1}. However, the global map of POC flux at 2000 m (Figure 10) shows high values (>1 mgC m^{-2} d^{-1}) at low latitudes, including equatorial Pacific regions and the Arabian Sea, and in the sub-Arctic regions. Intermediate values (~0.4–0.6 mgC m^{-2} d^{-1}) occurred at mid-latitudes and were slightly higher in coastal areas. Low values (<0.2 mgC m^{-2} d^{-1}) were found at most high latitudes. The 25th percentile, median, and 75th percentile of the POC flux at 2000 m were 0.09, 0.25, and 0.51 mgC m^{-2} d^{-1}, respectively, with a mean of 0.665 mgC m^{-2} d^{-1}.

The global map of particle transfer efficiency (Figure 11) shows very low values (<0.05) in the Southern Ocean and Northern Hemisphere high latitudes, which indicates that less than 5% of particulate organic carbon exported from the euphotic zone reaches 1000 m depth. Intermediate values (~0.15–0.25) were observed at mid-latitudes and

slightly higher around the coasts. Particle transfer efficiencies were high (>0.35) at low latitudes, especially in the Arabian Sea, equatorial Pacific, and Atlantic coastal areas. The 25th percentile, median, and 75th percentile of particulate transfer efficiency across the global ocean were 0.055, 0.092, and 0.20, respectively. The global particle transfer efficiency through the mesopelagic zone ranged between 0.012 and 0.66, with a mean of 0.13, indicating that globally an average of 13% of particulate organic carbon exported from the euphotic zone survives the remineralization process to reach 1000 m depth.

4 Discussion

4.1 POC sinking and remineralization rates

This study aims to test the hypothesis that remineralization length scales estimated using the POC sinking rates and remineralization rates approximate the observations derived from POC flux attenuation profiles. Eq. 6 shows that the POC sinking rate increases exponentially with increasing sea surface temperature and net primary production. This relationship is contrary to that of Iversen and Ploug (2013) who observed no direct influence of temperature on aggregate sinking speed. A possible explanation might be that this study used temperature and NPP simultaneously to predict POC sinking speed, and temperature and NPP may affect the sinking rate together. This relationship has not previously been described and provides a new insight into the relationship between the POC sinking rate and temperature and NPP.

Furthermore, Eq. 7 shows that the POC remineralization rate increases linearly with temperature, and the remineralization rate increases by a factor (Q_{10} coefficient) of ~2.6 for a 10 °C increase in temperature. This factor is slightly higher than that used in previous ocean biogeochemical models (e.g., Bopp et al., 2013) (~2) but lower than the laboratory estimate of 3.3 (Iversen & Ploug, 2013) and field-based estimate of 3.7 (Mazuecos et al., 2015). Therefore, this Q_{10} coefficient is roughly in the middle range of previous studies, contributing to the understanding of the temperature effect on the POC remineralization rate.

4.2 Remineralization length scales

For the RLS, medians and 25th percentiles of both the modelled RLS and observations were quite similar, while the distributions were different. As the observed RLS was generally higher than the modelled RLS, the modelled values predicted that 63% of the POC flux was remineralized at shallower depths, with more intense remineralization of organic carbon in the water column than observations. As shown in

Figure 2, when the sea surface temperature was less than 15 °C, observations were mainly larger than modelled RLS. This may be due to the fact that the modelled RLS is highly dependent on temperature and when the temperature is low, the model underestimates the RLS. Therefore, the modelled RLS fails to keep up with the observation. When the temperature was above 15 °C, the modelled RLS was mainly larger than the observation as the model overestimated the RLS at higher temperatures. Clustered data points with negative residuals between 15 and 20 °C are found to be located along the Guianas coast and at the Northwest Atlantic subtropical gyre where the annual temperature at 100 m is around 25 °C observed from Figure 5. As can be seen from Figure 3, when the NPP was greater than 2,000 mgC m^{-2} d^{-1}, observations were predominantly lower than modelled values, and the temperature of this fraction of data roughly ranged between 10 and 20 °C. This may be due to the model overestimating the RLS at higher NPP values and moderate temperatures. However, when NPP was below 2,000 mgC m^{-2} d^{-1}, NPP had little influence on the modelled RLS, with negative residuals corresponding to higher temperatures and positive residuals corresponding to lower temperatures. This suggests that the effect of temperature on RLS is more prominent than that of NPP.

4.3 Global maps

The medians of the modelled RLS and observations were quite similar, the means were close, the modelled RLS was on the right order of magnitude, and the discrepancy was only due to different distributions of the values. Therefore, global mapping projections were performed to bring Eq.6 and Eq.7 into global biogeochemical models and to investigate the particle transfer efficiency through the mesopelagic zone. The global map of RLS (Figure 6) shows a similar pattern to that in the annual sea surface temperature (Figure 5), indicating that the model is more dependent on temperature than NPP and that temperature plays a dominant role in explaining the attenuation of POC flux. However, this finding contrasts with previous studies (Marsay et al., 2015), which suggested that RLS decreases with increasing

temperature and that shallower remineralization occurs in warmer waters. A possible explanation for this might be that this study aims to investigate whether POC sinking and remineralization rates are enough to estimate RLS and did not include other factors in organic carbon sink.

The global maps of POC flux at 100 m (Figure 8) and 1000 m (Figure 9) show a similar geographical pattern, with high values occurring at high latitudes and around the coasts and low values occurring at low latitudes, which is close to the patterns in the global maps of NPP (Figure 4) and particle export efficiency (Figure 7). However, global maps of POC flux at 2000 m (Figure 10) and particle transfer efficiency (Figure 11) show high values at low latitudes and low values at most high latitudes, which is almost opposite to the patterns in Figures 8 and 9. This pattern is similar to that in Figure 5, suggesting that the effect of temperature on the transfer of POC in the mesopelagic zone is more significant than that of NPP.

For particle transfer efficiency, the global map of particle transfer efficiency (Figure 11) shows a pattern consistent with that of Henson et al. (2012) who found that the transfer efficiency to 2000 m was very low (~0.05) in the Southern Ocean and high (~0.25–0.4) in equatorial upwelling regions. However, their transfer efficiency distribution across the global ocean shows higher ratios than in Figure 11. In comparison, Figure 11 shows an opposite pattern to that of DeVries & Weber (2017) who observed the highest mesopelagic transfer efficiencies in the high-latitude Southern Ocean, North Pacific, and North Atlantic, and lowest transfer efficiencies in the subtropical gyre regions. Cram et al. (2018) exhibited a pattern of global transfer efficiency with low values occurring throughout the subtropical gyres and most of the tropics and high values occurring at high latitudes and tropical eastern boundary regions, which is inconsistent with the pattern demonstrated in Figure 11. Weber et al. (2016) revealed a global pattern of transfer efficiency to 1000 m depth with high values (~0.25) occurring at high latitudes and low values (~0.05) occurring in subtropical gyres, which is at odds with

the pattern shown in Figure 11.

4.4 Recommendations and limitations

Although the global pattern shown in Figure 11 is inconsistent with previous research, the range of mesopelagic transfer efficiency estimated in this study (0.012–0.66) is very close to previous studies (DeVries & Weber, 2017: 0.05–0.4; Cram et al., 2018: ~0.05–0.5; Weber et al., 2016: ~0.05–0.5). The difference between the modelled RLS and observations and the discrepancy in the global maps may be due to the fact that POC sinking and remineralization rates are not sufficient to explain the attenuation of organic carbon. Other critical factors in the biological pump should be included in the study of POC. For example, particle fragmentation plays a pivotal role in controlling the remineralization of sinking organic carbon. Briggs et al. (2020) proposed that particle fragmentation explained 50% of the POC attenuation with depth. Moreover, zooplankton diel vertical migration (DVM) has a significant impact on organic carbon sink. Aumont et al. (2018) estimated that the active flux of carbon driven by DVM was 1.05 ± 0.15 PgC yr^{-1}, approximately 18% of the passive flux due to sinking particles. Archibald et al. (2019) found that the average proportional contribution of DVM activity to total respiration in the mesopelagic zone was 0.16 ± 0.06. Zooplankton grazing is also an essential contributor to the biological pump, converting most organic carbon fixed by phytoplankton through photosynthesis into CO_2 in the upper ocean, where it can be reused or released back into the atmosphere (Nowicki et al., 2022). Therefore, these important factors, including particle fragmentation, zooplankton grazing, and diel vertical migration, should be considered together with the POC sinking rate and remineralization rate in future research. This may make the modelled RLS closer to the observation and more accurately describe the attenuation of POC.

The results of this study may be limited by the fact that only linear regression was fitted to the data, thus potentially biasing the estimates of RLS. Furthermore, collecting samples from the vast oceans is difficult, with sediment traps typically operating for

weeks to months to record the changes in sinking flux over time. Preserving collected samples during deployments is also challenging as samples are susceptible to decomposition and consumption by zooplankton (Buesseler et al., 2007). The particle type for most data collected in Tables 1 and 2 is sinking phytodetrital aggregates. Since 85% of the gravitational pump is due to zooplankton fecal pellets, 15% is due to sinking phytoplankton aggregates (Nowicki et al., 2022), and fecal pellets generally have higher sinking rates than aggregates (Fischer and Karakaş, 2009), there might be deviations in estimating the POC sinking rates. Overall, this study contributes to a clearer understanding of the attenuation of particulate organic carbon.

5 Conclusion

Since the remineralization length scale is not well parameterized in ocean biogeochemical models, this thesis aims to use temperature and NPP to investigate whether the POC sinking rate and remineralization rate are sufficient to explain the attenuation of POC in the global ocean. POC sinking and remineralization rates and relevant information were collected from published papers, and linear models were fitted to the compiled data, followed by estimating the RLS based on the functions derived from linear regressions using sea temperatures and NPP as inputs. A significant difference between the modelled RLS and observations was observed, suggesting that the POC sinking rate and remineralization rate are not sufficient to explain the attenuation of POC in the water column. However, median values of the modelled RLS and observations were quite similar, mean values were close, the modelled RLS was on the correct order of magnitude, and the discrepancy was only due to different distributions of values. Therefore, global mapping projections were performed to bring the functions that use temperature and NPP to predict the POC sinking rate and remineralization rate into global biogeochemical models. The global map of transfer efficiency through the mesopelagic zone shows high values in tropical and subtropical regions and low values at high latitudes, with a mean of 0.13, indicating that globally an average of 13% of POC exported from the euphotic zone survives the remineralization to reach 1000 m depth. Although the global pattern is inconsistent with previous research, the range of mesopelagic transfer efficiency (0.012–0.66) is very close to previous studies. In summary, this study contributes to the understanding of the attenuation of POC and mesopelagic particle transfer efficiency. Future studies should consider particle fragmentation, zooplankton grazing, and diel vertical migration along with the POC sinking and remineralization to investigate the attenuation of POC.

Data and Code Availability

Data can be accessed from:

https://github.com/JunyueZhang/CMEECourseWork/tree/master/Master__Project/data

Code can be accessed from:

https://github.com/JunyueZhang/CMEECourseWork/tree/master/Master__Project/code

Acknowledgments

I'm incredibly grateful to my supervisors, Dr Emma Cavan and Prof Stephanie Henson in the National Oceanography Centre, for their patience and excellent guidance and helpful comments during this project. I have been blessed to have such two professional and knowledgeable supervisors who are very nice and passionate about research. And I am very grateful to Dr B.B. Cael in the National Oceanography Centre for providing the data for the POC sinking rates. I am very grateful to my parents for their financial support, which enabled me to have the opportunity to study at Imperial College which I had dreamed of for a long time.

References

Alldredge, A. L., & Gotschalk, C. C. (1989). Direct observations of the mass flocculation of diatom blooms: characteristics, settling velocities and formation of diatom aggregates. Deep Sea Research Part A. Oceanographic Research Papers, 36(2), 159-171.

Alonso-González, I. J., Arístegui, J., Lee, C., Sanchez-Vidal, A., Calafat, A., Fabrés, J., ... & Benítez-Barrios, V. (2010). Role of slowly settling particles in the ocean carbon cycle. Geophysical research letters, 37(13).

Archibald, K. M., Siegel, D. A., & Doney, S. C. (2019). Modeling the impact of zooplankton diel vertical migration on the carbon export flux of the biological pump. Global Biogeochemical Cycles, 33(2), 181-199.

Aumont, O., Maury, O., Lefort, S., & Bopp, L. (2018). Evaluating the potential impacts of the diurnal vertical migration by marine organisms on marine biogeochemistry. Global Biogeochemical Cycles, 32(11), 1622-1643.

Barange, M., Butenschön, M., Yool, A., Beaumont, N., Fernandes, J. A., Martin, A. P., & Allen, J. I. (2017). The cost of reducing the North Atlantic Ocean biological carbon pump. Frontiers in Marine Science, 3, 290.

Basu, S., & Mackey, K. R. (2018). Phytoplankton as key mediators of the biological carbon pump: Their responses to a changing climate. Sustainability, 10(3), 869.

Behrenfeld, M. J., & Falkowski, P. G. (1997). Photosynthetic rates derived from satellite-based chlorophyll concentration. Limnology and oceanography, 42(1), 1-20.

Bidle, K. D., Manganelli, M., & Azam, F. (2002). Regulation of oceanic silicon and carbon preservation by temperature control on bacteria. Science, 298(5600), 1980-1984.

Bienfang, P. K. (1980). Phytoplankton sinking rates in oligotrophic waters off Hawaii, USA. Marine Biology, 61(1), 69-77.

Bishop, J. K. (2009). Autonomous observations of the ocean biological carbon pump. Oceanography, 22(2), 182-193.

Bopp, L., Resplandy, L., Orr, J. C., Doney, S. C., Dunne, J. P., Gehlen, M., ... & Vichi, M. (2013). Multiple stressors of ocean ecosystems in the 21st century: projections with CMIP5 models. Biogeosciences, 10(10), 6225-6245.

Boyd, P. W. (2015). Toward quantifying the response of the oceans' biological pump to climate change. Frontiers in Marine Science, 2, 77.

Boyd, P. W., & Trull, T. W. (2007). Understanding the export of biogenic particles in oceanic waters: Is there consensus?. Progress in Oceanography, 72(4), 276-312.

Boyd, P. W., Claustre, H., Levy, M., Siegel, D. A., & Weber, T. (2019). Multi-faceted particle pumps drive carbon sequestration in the ocean. Nature, 568(7752), 327-335.

Briggs, N., Dall'Olmo, G., & Claustre, H. (2020). Major role of particle fragmentation in regulating biological sequestration of CO2 by the oceans. Science, 367(6479), 791-793.

Buesseler, K. O., Antia, A. N., Chen, M., Fowler, S. W., Gardner, W. D., Gustafsson, O., ... & Trull, T. (2007). An assessment of the use of sediment traps for estimating upper ocean particle fluxes. Journal of Marine Research, 65(3), 345-416.

Cael, B. B., Cavan, E. L., & Britten, G. L. (2021). Reconciling the size-dependence of marine particle sinking speed. Geophysical Research Letters, 48(5), e2020GL091771.

Cavan, E. L., Belcher, A., Atkinson, A., Hill, S. L., Kawaguchi, S., McCormack, S., ... & Boyd, P. W. (2019). The importance of Antarctic krill in biogeochemical cycles. Nature communications, 10(1), 1-13.

Cavan, E. L., Henson, S. A., Belcher, A., & Sanders, R. (2017). Role of zooplankton in determining the efficiency of the biological carbon pump. Biogeosciences, 14(1), 177-186.

Cavan, E. L., Trimmer, M., Shelley, F., & Sanders, R. (2017). Remineralization of particulate organic carbon in an ocean oxygen minimum zone. Nature Communications, 8(1), 1-9.

Chisholm, S. W. (1995). The iron hypothesis: Basic research meets environmental policy. Reviews of Geophysics, 33(S2), 1277-1286.

Cram, J. A., Weber, T., Leung, S. W., McDonnell, A. M., Liang, J. H., & Deutsch, C.

(2018). The role of particle size, ballast, temperature, and oxygen in the sinking flux to the deep sea. Global Biogeochemical Cycles, 32(5), 858-876.

Davison, P. C., Checkley Jr, D. M., Koslow, J. A., & Barlow, J. (2013). Carbon export mediated by mesopelagic fishes in the northeast Pacific Ocean. Progress in Oceanography, 116, 14-30.

Devol, A. H., & Hartnett, H. E. (2001). Role of the oxygen-deficient zone in transfer of organic carbon to the deep ocean. Limnology and Oceanography, 46(7), 1684-1690.

DeVries, T., & Weber, T. (2017). The export and fate of organic matter in the ocean: New constraints from combining satellite and oceanographic tracer observations. Global Biogeochemical Cycles, 31(3), 535-555.

Doney, S. C., Lindsay, K., Caldeira, K., Campin, J. M., Drange, H., Dutay, J. C., ... & Yool, A. (2004). Evaluating global ocean carbon models: The importance of realistic physics. Global Biogeochemical Cycles, 18(3).

Dunne, J. P., Armstrong, R. A., Gnanadesikan, A., & Sarmiento, J. L. (2005). Empirical and mechanistic models for the particle export ratio. Global Biogeochemical Cycles, 19(4).

Fischer, G., & Karakaş, G. (2009). Sinking rates and ballast composition of particles in the Atlantic Ocean: implications for the organic carbon fluxes to the deep ocean. biogeosciences, 6(1), 85-102.

Fowler, S. W., & Small, L. F. (1972). Sinking rates of euphausiid fecal pellets. Limnology and Oceanography, 17(2), 293-296.

Francois, R., Honjo, S., Krishfield, R., & Manganini, S. (2002). Factors controlling the flux of organic carbon to the bathypelagic zone of the ocean. Global Biogeochemical Cycles, 16(4), 34-1.

Guidi, L., Stemmann, L., Jackson, G. A., Ibanez, F., Claustre, H., Legendre, L., ... & Gorskya, G. (2009). Effects of phytoplankton community on production, size, and export of large aggregates: A world-ocean analysis. Limnology and Oceanography, 54(6), 1951-1963.

Helmke, P., Romero, O., & Fischer, G. (2005). Northwest African upwelling and its

effect on offshore organic carbon export to the deep sea. Global Biogeochemical Cycles, 19(4).

Henson, S. A., Sanders, R., & Madsen, E. (2012). Global patterns in efficiency of particulate organic carbon export and transfer to the deep ocean. Global Biogeochemical Cycles, 26(1).

Henson, S. A., Sanders, R., Madsen, E., Morris, P. J., Le Moigne, F., & Quartly, G. D. (2011). A reduced estimate of the strength of the ocean's biological carbon pump. Geophysical Research Letters, 38(4).

Hutchins, D. A., & Fu, F. (2017). Microorganisms and ocean global change. Nature microbiology, 2(6), 1-11.

Iversen, M. H., & Ploug, H. (2010). Ballast minerals and the sinking carbon flux in the ocean: carbon-specific respiration rates and sinking velocity of marine snow aggregates. Biogeosciences, 7(9), 2613-2624.

Iversen, M. H., & Ploug, H. (2013). Temperature effects on carbon-specific respiration rate and sinking velocity of diatom aggregates–potential implications for deep ocean export processes. Biogeosciences, 10(6), 4073-4085.

Iversen, M. H., Nowald, N., Ploug, H., Jackson, G. A., & Fischer, G. (2010). High resolution profiles of vertical particulate organic matter export off Cape Blanc, Mauritania: Degradation processes and ballasting effects. Deep Sea Research Part I: Oceanographic Research Papers, 57(6), 771-784.

Kim, J. M., Lee, K., Shin, K., Yang, E. J., Engel, A., Karl, D. M., & Kim, H. C. (2011). Shifts in biogenic carbon flow from particulate to dissolved forms under high carbon dioxide and warm ocean conditions. Geophysical Research Letters, 38(8).

Klaas, C., & Archer, D. E. (2002). Association of sinking organic matter with various types of mineral ballast in the deep sea: Implications for the rain ratio. Global biogeochemical cycles, 16(4), 63-1.

Locarnini, R. A., A. V. Mishonov, O. K. Baranova, T. P. Boyer, M. M. Zweng, H. E. Garcia, J. R. Reagan, D. Seidov, K. Weathers, C. R. Paver, and I. Smolyar (2018). World Ocean Atlas 2018, Volume 1: Temperature. A. Mishonov Technical Ed.; NOAA Atlas

NESDIS 81, 52pp.

Marsay, C. M., Sanders, R. J., Henson, S. A., Pabortsava, K., Achterberg, E. P., & Lampitt, R. S. (2015). Attenuation of sinking particulate organic carbon flux through the mesopelagic ocean. Proceedings of the National Academy of Sciences, 112(4), 1089-1094.

Martin, J. H., Knauer, G. A., Karl, D. M., & Broenkow, W. W. (1987). VERTEX: carbon cycling in the northeast Pacific. Deep Sea Research Part A. Oceanographic Research Papers, 34(2), 267-285.

Mayor, D. J., Gentleman, W. C., & Anderson, T. R. (2020). Ocean carbon sequestration: Particle fragmentation by copepods as a significant unrecognised factor? Explicitly representing the role of copepods in biogeochemical models may fundamentally improve understanding of future ocean carbon storage. BioEssays, 42(12), 2000149.

Mazuecos, I. P., Aristegui, J., Vazquez-Dominguez, E., Ortega-Retuerta, E., Gasol, J. M., & Reche, I. (2015). Temperature control of microbial respiration and growth efficiency in the mesopelagic zone of the South Atlantic and Indian Oceans. Deep Sea Research Part I: Oceanographic Research Papers, 95, 131-138.

Mouw, C. B., Barnett, A., McKinley, G. A., Gloege, L., and Pilcher, D. (2016). Global ocean particulate organic carbon flux merged with satellite parameters, Earth Syst. Sci. Data, 8, 531–541, https://doi.org/10.5194/essd-8-531-2016.

Mouw, Colleen B, Barnett, Audrey, McKinley, Galen A, Gloege, Lucas, Pilcher, Darren (2016). Global ocean flux rates. PANGAEA, https://doi.org/10.1594/PANGAEA.855594, In supplement to: Mouw, CB et al. (2016). Global ocean particulate organic carbon flux merged with satellite parameters. Earth System Science Data, 8(2), 531-541, https://doi.org/10.5194/essd-8-531-2016.

Mouw, Colleen B, Barnett, Audrey, McKinley, Galen A, Gloege, Lucas, Pilcher, Darren (2016). Global Ocean Particulate Organic Carbon flux merged with satellite parameters. PANGAEA, https://doi.org/10.1594/PANGAEA.855600, Supplement to: Mouw, CB et al. (2016). Global ocean particulate organic carbon flux merged with satellite parameters. Earth System Science Data, 8(2), 531-541,

https://doi.org/10.5194/essd-8-531-2016.

Nowicki, M., DeVries, T., & Siegel, D. A. (2022). Quantifying the carbon export and sequestration pathways of the ocean's biological carbon pump. Global Biogeochemical Cycles, 36(3), e2021GB007083.

Passow, U., & Carlson, C. A. (2012). The biological pump in a high CO2 world. Marine Ecology Progress Series, 470, 249-271.

Ploug, H., & Grossart, H. P. (2000). Bacterial growth and grazing on diatom aggregates: Respiratory carbon turnover as a function of aggregate size and sinking velocity. Limnology and Oceanography, 45(7), 1467-1475.

Robinson, C., Steinberg, D. K., Anderson, T. R., Arístegui, J., Carlson, C. A., Frost, J. R., ... & Zhang, J. (2010). Mesopelagic zone ecology and biogeochemistry–a synthesis. Deep Sea Research Part II: Topical Studies in Oceanography, 57(16), 1504-1518.

Sanders, R., Henson, S. A., Koski, M., Christina, L. D. L. R., Painter, S. C., Poulton, A. J., ... & Martin, A. P. (2014). The biological carbon pump in the North Atlantic. Progress in Oceanography, 129, 200-218.

Siegel, D. A., Buesseler, K. O., Doney, S. C., Sailley, S. F., Behrenfeld, M. J., & Boyd, P. W. (2014). Global assessment of ocean carbon export by combining satellite observations and food‐web models. Global Biogeochemical Cycles, 28(3), 181-196.

Siegel, D. A., Granata, T. C., Michaels, A. F., & Dickey, T. D. (1990). Mesoscale eddy diffusion, particle sinking, and the interpretation of sediment trap data. Journal of Geophysical Research: Oceans, 95(C4), 5305-5311.

Smetacek, V. S. (1985). Role of sinking in diatom life-history cycles: ecological, evolutionary and geological significance. Marine biology, 84(3), 239-251.

Steinberg, D. K., & Landry, M. R. (2017). Zooplankton and the ocean carbon cycle. Annual review of marine science, 9(1), 413-444.

Turner, J. T. (2002). Zooplankton fecal pellets, marine snow and sinking phytoplankton blooms. Aquatic microbial ecology, 27(1), 57-102.

Turner, J. T. (2015). Zooplankton fecal pellets, marine snow, phytodetritus and the ocean’s biological pump. Progress in Oceanography, 130, 205-248.

Weber, T., Cram, J. A., Leung, S. W., DeVries, T., & Deutsch, C. (2016). Deep ocean nutrients imply large latitudinal variation in particle transfer efficiency. Proceedings of the National Academy of Sciences, 113(31), 8606-8611.

Supplementary Material

Table 1 shows the compiled table used to make the linear regression for the POC sinking rate.

Citation	Location	Method	Particle Type	Start Time	End Time
Alldredge & Gotschalk, 1989	Santa Barbara Channel	In situ (scuba+dye)	Diatom aggregates	1986	1988
Alldredge & Gotschalk, 1988	California Current	In situ (scuba+dye)	Aggregates	1986 March	1986 June
Azetsu-Scott & Johnson, 1991	Bedford Basin	Settling column	Aggregates	1989/10/31	1989/11/2
Iversen et al., 2010	Cape Blanc (Mauritania)	Vertical flow system	Ballasted aggregates	2007/3/23	2007/3/29
Belcher et al., 2016	PAP	Flow chamber	Aggregates	2015/6/20	2015/7/8
Cavan et al., 2018	ETNP (Guatemala)	FlowCAM	Fecal pellets	2013/12/28	2014/2/10
Diercks & Asper, 1997	Black Sea	MASCOT	Aggregates	1988/4/24	1988/5/3
Gibbs, 1985	Chesapeake bay	Settling column	Ballasted aggregates	1985	1985
Kajihara, 1971	Kuroshio	Settling column	Aggregates	1969/9/3	1969
Nowald et al., 2009	Cape Blanc (Mauritania)	In situ chamber	Ballasted aggregates	2008/4/26	2009/3/28
Shanks & Trent, 1980	Monterey Bay (+NE Atl.)	In situ (scuba)	Aggregates	1980	1980
Small et al., 1979	Ligurian Sea	Settling column	Fecal pellets	1978/2	1978/5
Smayda, 1969	Naragansett Bay	Settling column	Fecal pellets	1969	1969
Syvitski et al., 1995	Bedford Basin	Floc camera assembly	Ballasted aggregates	1989	1990
Van der Jagt et al., 2018	Cape Blanc (Mauritania)	Vertical flow system	Aggregates	2015/2/15	2015/3/3

Latitude	Longitude	Depth (m)	Temperature (°C)	NPP (mg C / m^2 / day)	SV (m/d)
34.2	-120	15	14.39	2872.137273	120
33.7	-118.3	15	14.97	1757.06	63.2
44.7	-63.63	15	8.991	2684.95	89.8
21	-19	15	19.335	1660.42	142
49	-16.5	36-500	12.251	2136.96	29.8
13	-91	10-350	14.829	551.985	52
43	34	688	8.898	881.922	9.03
39.5	-76	10	12.736	2571.234545	25
42.3	140.9	30, 42	17.285	914.13	65.9
20	-18	1210	5.628	2641.319091	44.3
36.63	-121.87	10	12.548	3418.402636	60
43.6	7.43	10	15.706	866.637	65.8
41.45	-71.45	10	11.839	2533.187143	147
44.69	-63.64	35	4.939	2235.76	21.6
21	-20	20	21.294	1894.14	191

Table 1 – Compiled table used to make the linear regression for the POC sinking rate.

Table 2 shows the compiled table used to make the linear regression for the POC remineralization rate.

Data Contributor	Start Time	End Time	Latitude	Longitude	Location	Depth (m)
Iversen et al., 2010	2007/3/23	2007/3/29	21	-20	NE Atlantic	
Ploug et al., 1999	1997/6/6	1997/6/28	47	-90	NE Pacific	15
McDonnell et al., 2015	2009/3/5	2009/3/7	-64	-65	Long-Term Ecological Research	50
Iversen M. & Ploug H, 2013			56	2.7	North Sea	
Belcher et al., 2016	Austral spring 2014	Austral spring 2014	-55	-41	Scotia Sea	200
Iversen et al., 2017	2012/1/29	2012/2/17	-51	-40	Southern Atlantic Ocean	300
Ploug and Bergkvist, 2015 García-Martín, E. E. et al., 2021	2014/11, 2015/4, 2015/7	2014/11, 2015/4, 2015/7	48	-9	Celtic Sea	200

k (d-1)	Temperature (°C)	NPP(mg C / m^2 / day)	Method	Type
0.13	18	2027.97	O2 diffusion in flow chamber	Aggregates produced using roller tanks
0.12	17	4812.48	O2 diffusion in flow chamber	Detritus
0.01	0.207	237.595	RESPIRE sediment traps	Krill and salp fecal pellets, diatoms, and aggregates
0.03	4	1139.582	O2 diffusion in flow chamber	Aggregates produced using roller tanks
0.028	4	252.075	O2 diffusion in flow chamber	Euphausia superba Fecal pellets
0.04	3	595.233	O2 diffusion in flow chamber	Salp fecal pellets
0.065	10		O2 diffusion in flow chamber	Aggregates produced using roller tanks (Hypoxic conditions)
0.08	11.546	1663.64	Assay incubation measuring O2 decline	Fast-sinking Detritus

Table 2 – Compiled table used to make the linear regression for the POC remineralization rate.

Several linear regressions were made to estimate the POC sinking rate as listed below:

$w = -19.314 + 7.239 \times SST$ [1]

The R-squared is 0.3993, p-value is 0.0115, and AIC value is 158.92.

$w = 13.6e^{(0.11 \times SST)}$ [2]

The R-squared is 0.3811, p-value is 0.0142, and AIC value is 34.54.

$w = -90.596 + 8.85 \times SST + 0.025 \times NPP$ [3]

The R-squared is 0.55, p-value is 0.008, and AIC value is 156.59.

$w = 3.867exp^{(0.139 \times SST + 0.00045 \times NPP)}$ [4]

The R-squared is 0.5739, p-value is 0.006, and AIC value is 30.95. Since a lower AIC score is better, equation 4 was chosen to predict the POC sinking rate using sea surface temperatures and net primary production data as inputs. Figure 1 shows the modelled POC sinking rates derived from equation 4 versus observed POC sinking rates.

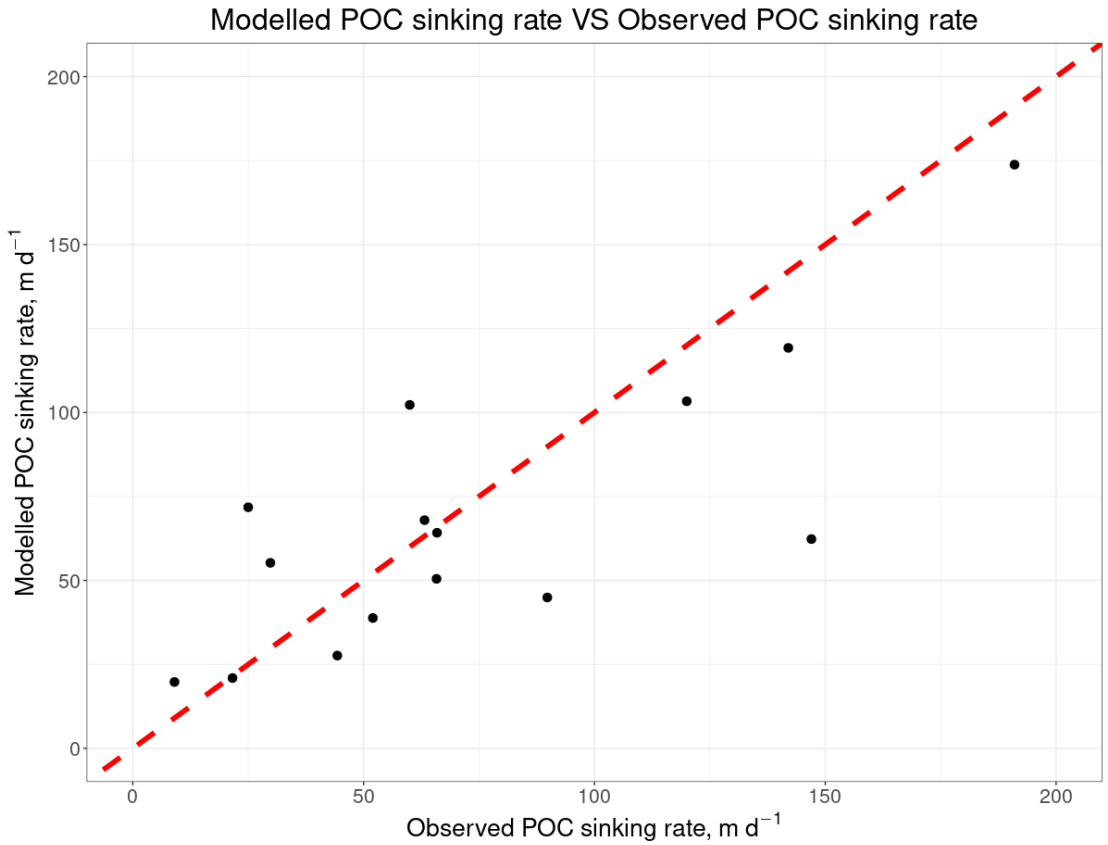

Figure 1 - Comparison of modelled POC sinking rates with observed values searched from the literature. The x-axis indicates the observed POC sinking rates, the y-axis

indicates the modelled values derived from equation 4, and the red dashed line indicates y=x.

Similarly, several linear regressions were made to estimate the POC remineralization rate as listed below:

$k = 0.00756 + 0.00653 \times SST$ [5]

The R-squared is 0.9774, p-value is 3.619e-06, and AIC value is -52.6.

$k = 0.017e^{(0.12 \times SST)}$ [6]

The R-squared is 0.8787, p-value is 0.00058, and AIC value is 8.36.

$k = 0.009829 + 0.006435 \times SST + 3.277 \times 10^{-7} \times NPP$ [7]

The R-squared is 0.9831, p-value is 0.0022, and AIC value is -36.54.

$k = 0.0165exp^{(0.1276 \times SST - 3.288 \times 10^{-5} \times NPP)}$ [8]

The R-squared is 0.8775, p-value is 0.043, and AIC value is 11.18. Since lower AIC scores are better, equation 5 was chosen to predict the POC remineralization rate using sea surface temperatures as inputs. As shown in Figure 2, the POC remineralization rate is highly linearly correlated with sea surface temperature. Figure 3 shows the modelled POC remineralization rates derived from equation 5 versus observed POC remineralization rates.

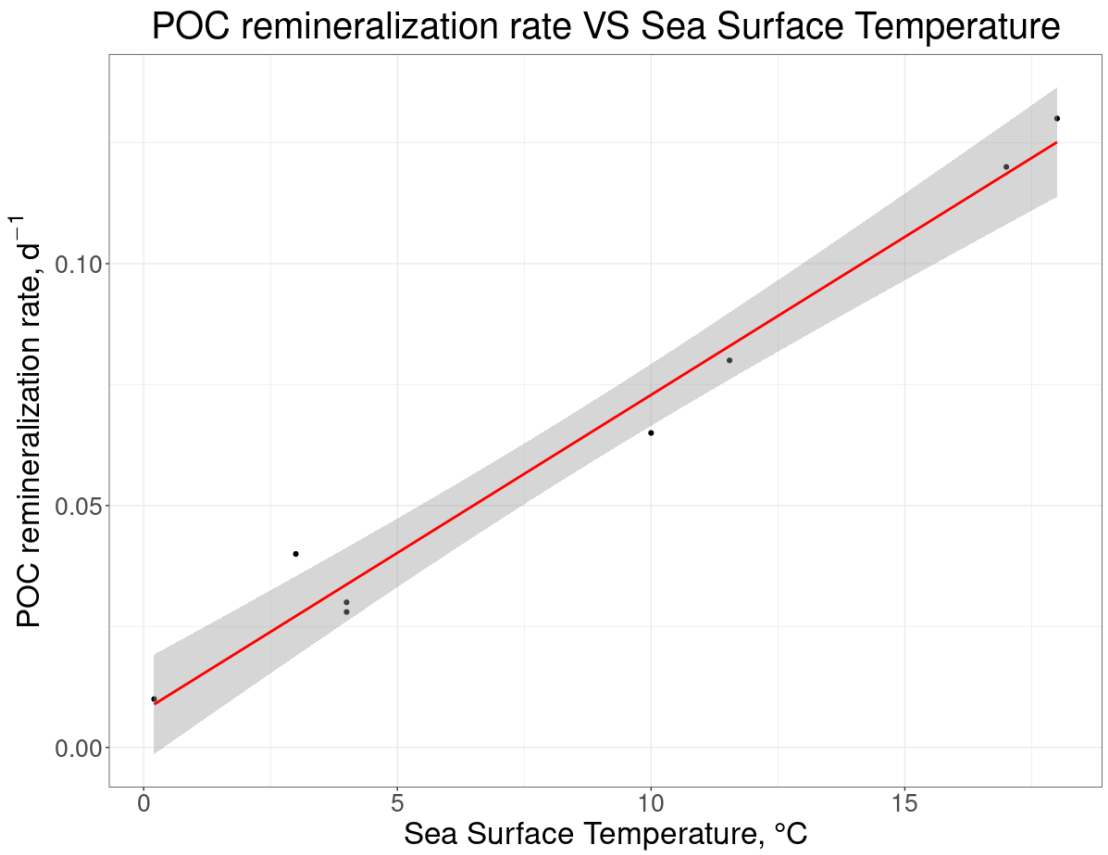

Figure 2 – Variation of POC remineralization rate with sea surface temperature. The red line indicates the linear function of equation 5, and the grey zone indicates the 95% confidence interval for predictions from the linear regression.

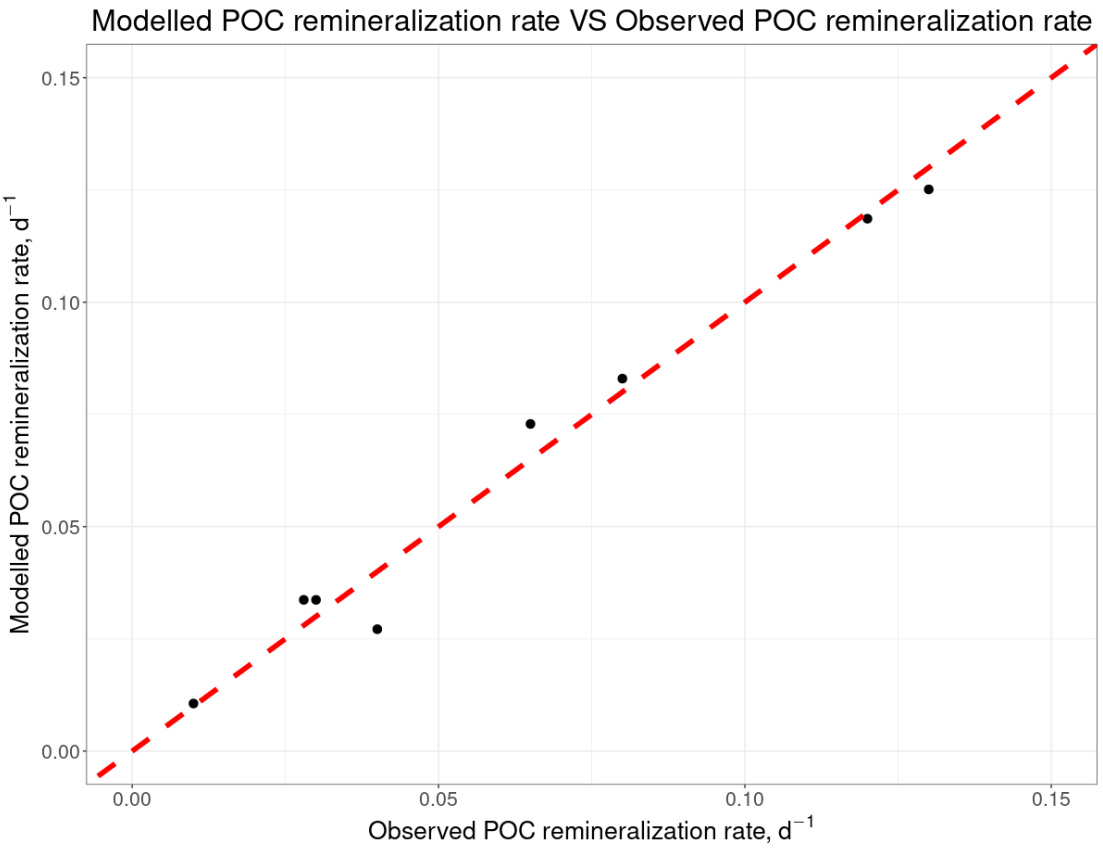

Figure 3 - Comparison of modelled POC remineralization rates derived from equation 5 with observed values searched from the literature. The x-axis indicates the observed POC remineralization rates, the y-axis indicates the modelled POC remineralization rates, and the red dashed line indicates y=x.

Figures 4 and 5 show the histograms of the observed RLS and modelled RLS, respectively.

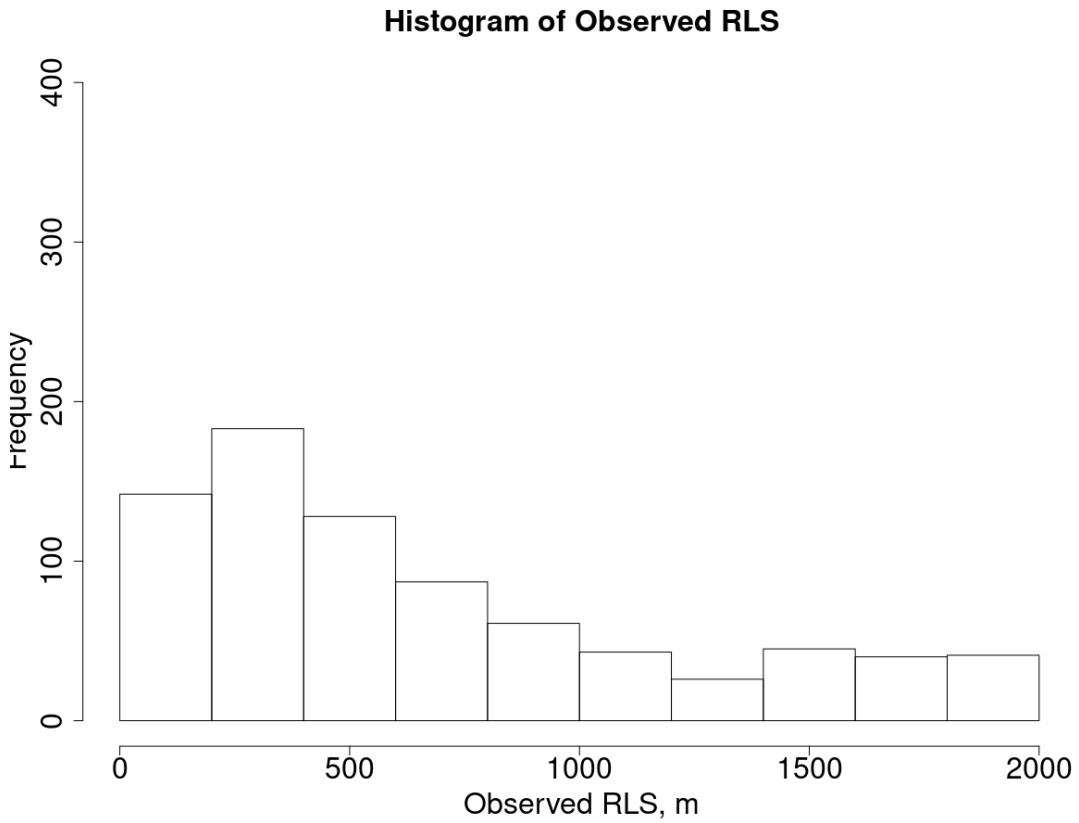

Figure 4 - Histogram of the observed RLS.

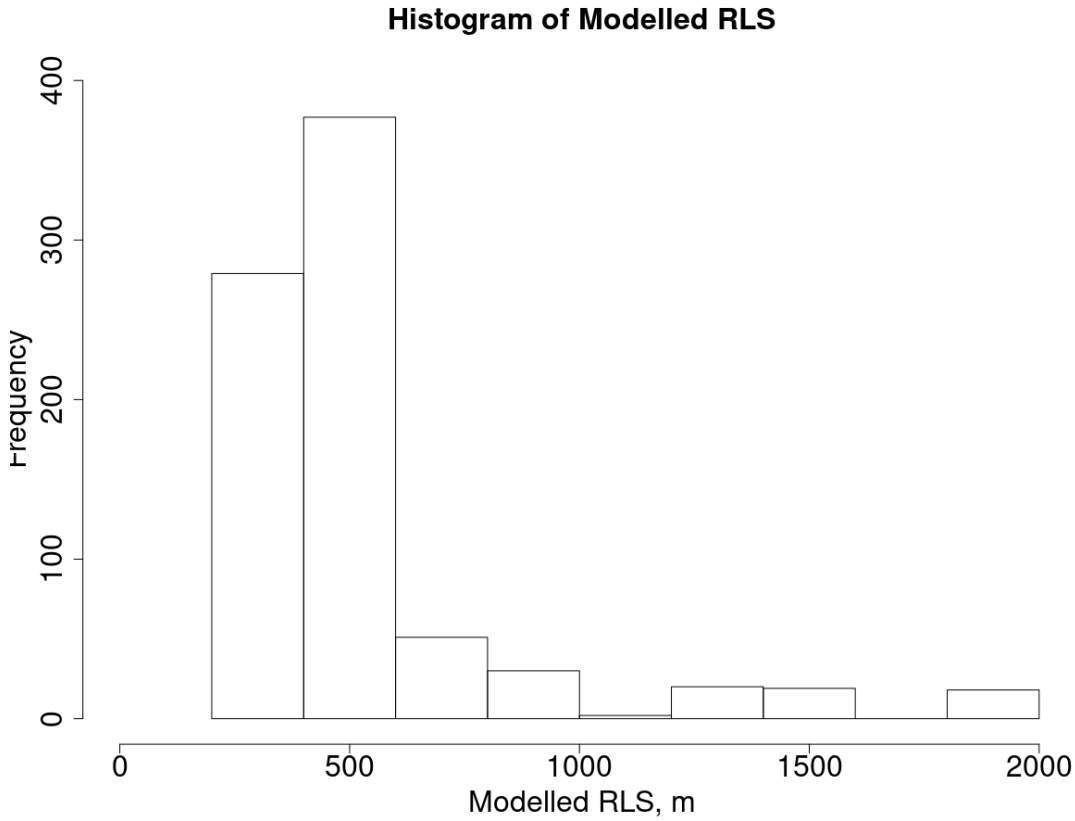

Figure 5 - Histogram of the modelled RLS.

Figure 6 displays an example plot of POC attenuation in the water column from the global dataset compiled by Mouw et al. (2016). POC fluxes were measured using sediment traps at 18°N, 64°W for 14 days between 11 November 2004 and 25 November 2004.

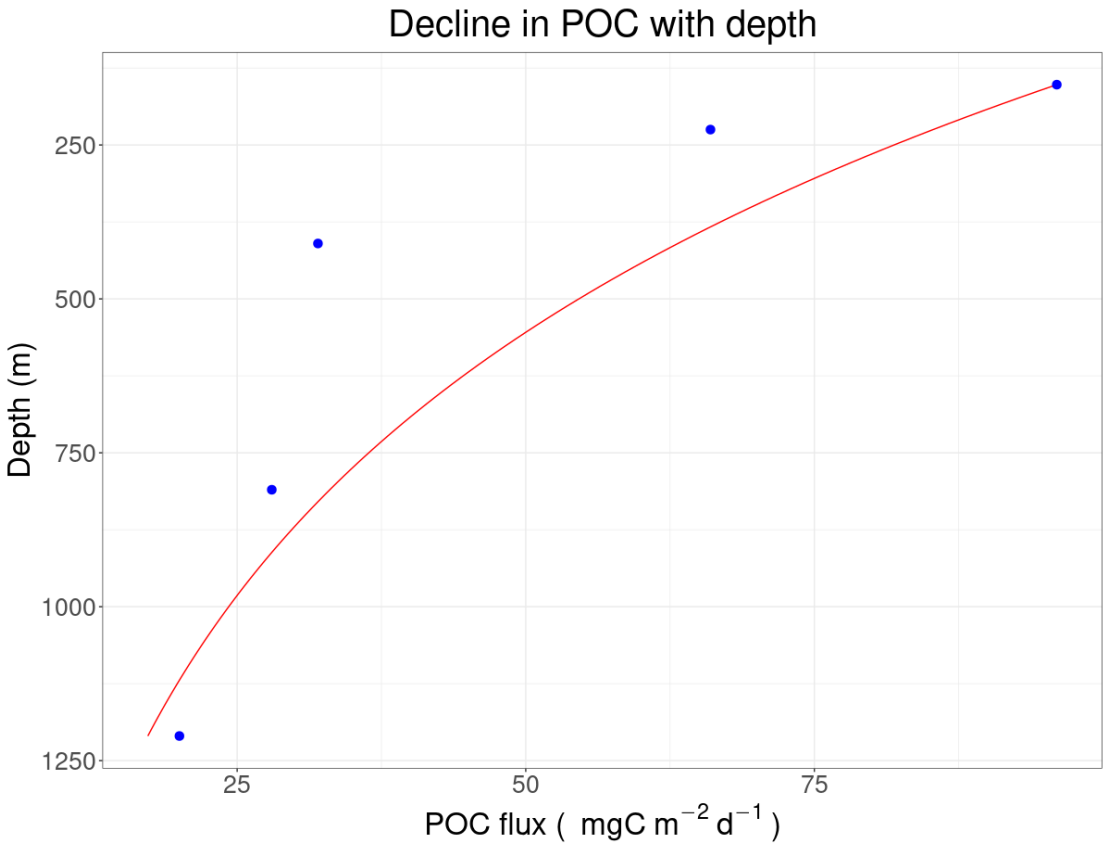

Figure 6 – Example plot of POC attenuation in the water column from the global dataset compiled by Mouw et al. (2016). The blue dots indicate POC fluxes with depth, and the red curve indicates the exponential function of equation 2 with the shallowest depth as the reference.

Figure 7 shows the deployment locations of the Mouw et al. (2016) dataset on the global map.

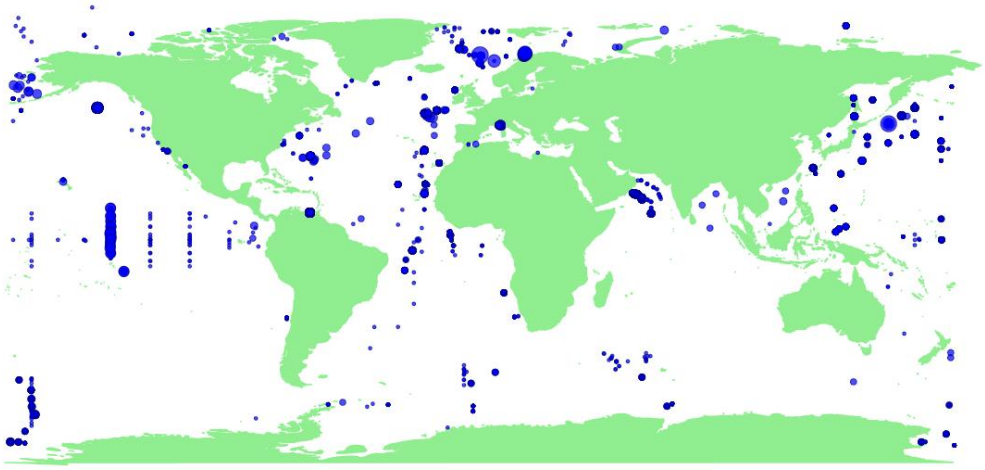

Figure 7 – Global map with locations of the Mouw et al. (2016) dataset. The size of the data points corresponds to the number of deployments at that location.

In comparison, Figure 8 shows the global particle transfer efficiency mapped by Henson et al. (2012) to 2000 m depth.

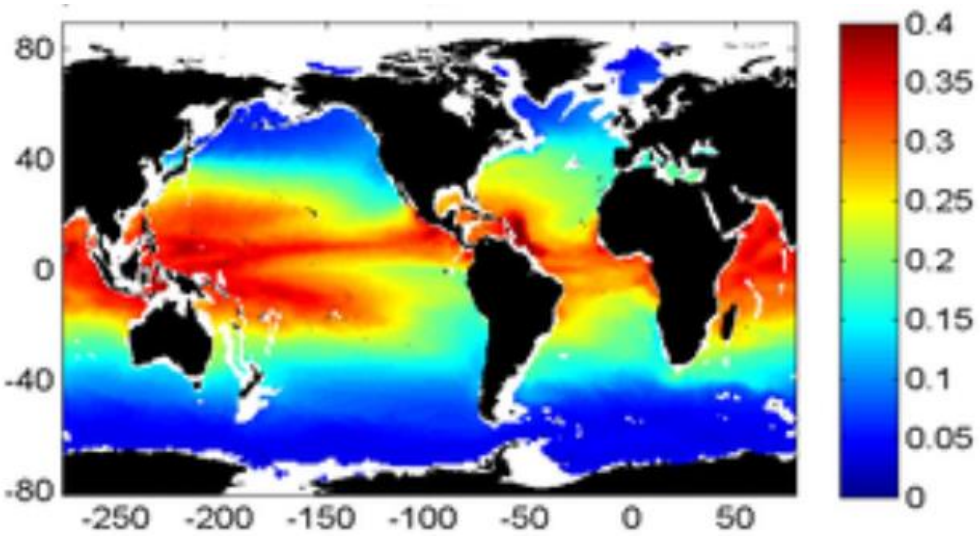

Figure 8 - Global particle transfer efficiency mapped by Henson et al. (2012) to 2000 m depth.

Figure 9 shows a global map of mesopelagic transfer efficiency to 1000 m depth produced by DeVries & Weber (2017).

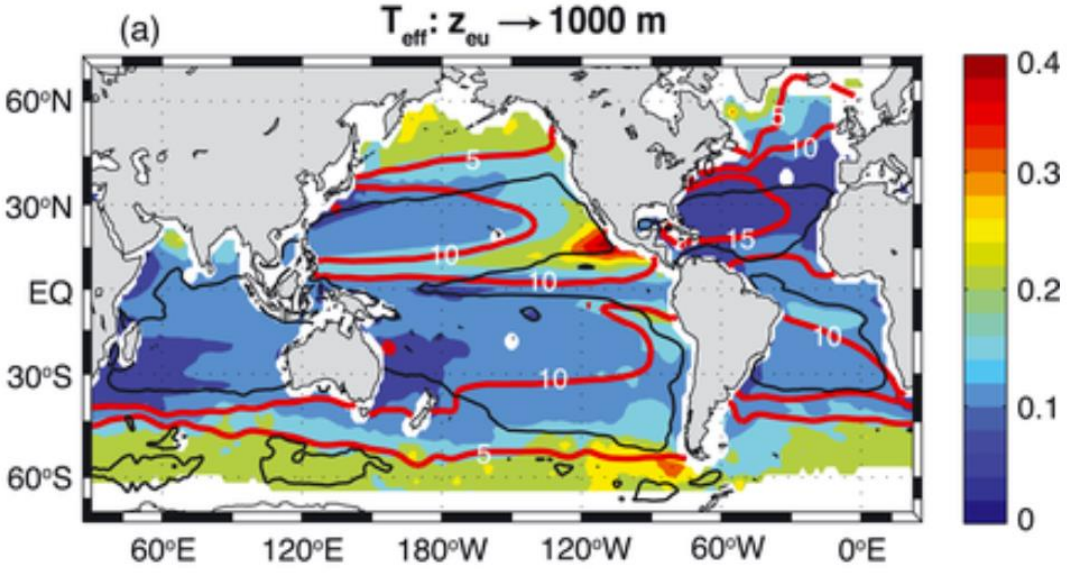

Figure 9 - Global mesopelagic transfer efficiency to 1000 m depth mapped by DeVries & Weber (2017).

Figure 10 shows a global map of transfer efficiency of organic matter between the euphotic zone and 1000 m produced by Cram et al. (2018).

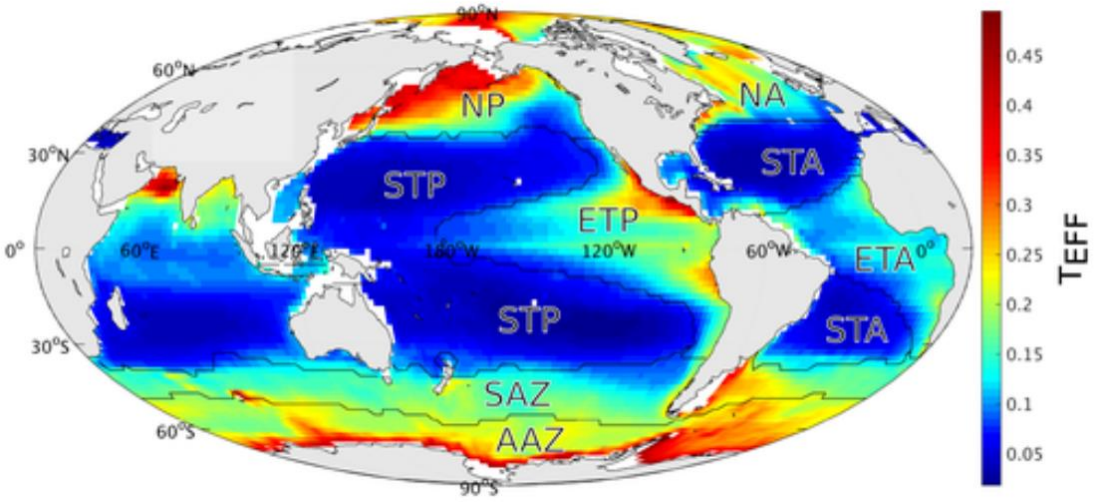

Figure 10 - Global transfer efficiency of organic matter between the euphotic zone and 1000 m mapped by Cram et al. (2018).

Figure 11 shows a global map of transfer efficiency to 1000 m produced by Weber et al. (2016).

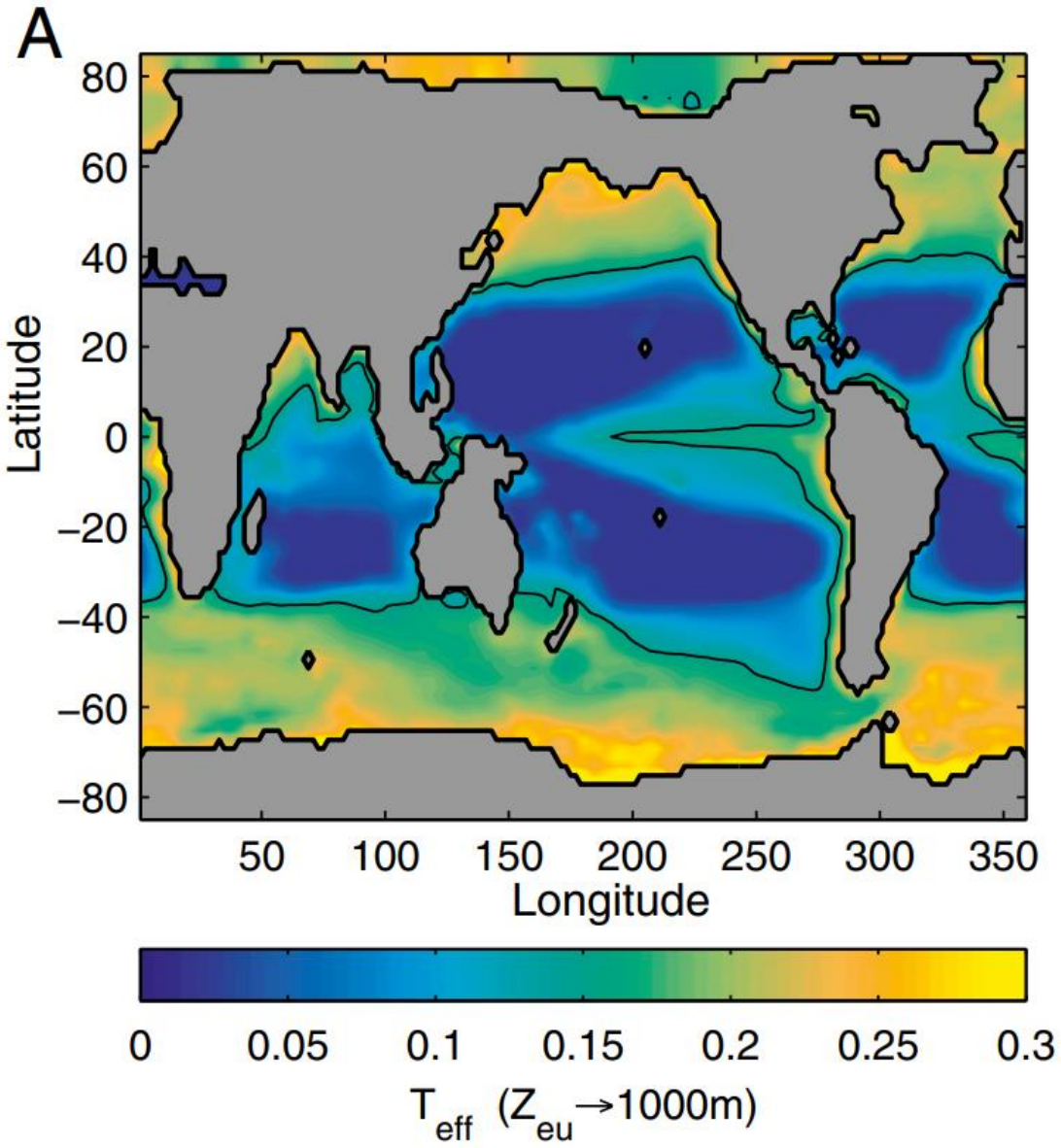

Figure 11 - Global transfer efficiency to 1000 m mapped by Weber et al. (2016).

Figure 12 shows a flow chart for the project.

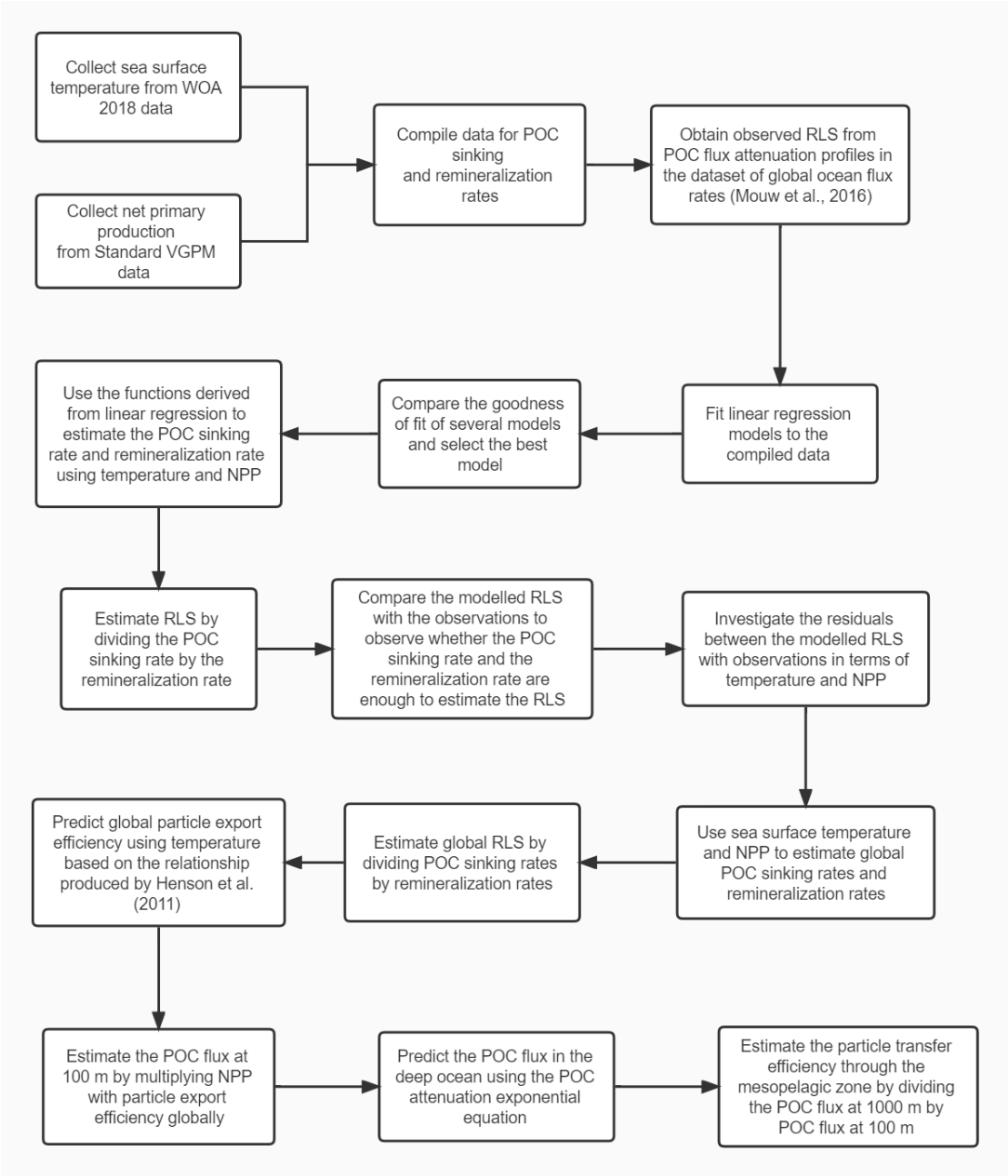

Figure 12 - Flow chart for the project.

References for Supplementary Material

Cram, J. A., Weber, T., Leung, S. W., McDonnell, A. M., Liang, J. H., & Deutsch, C. (2018). The role of particle size, ballast, temperature, and oxygen in the sinking flux to the deep sea. Global Biogeochemical Cycles, 32(5), 858-876.

DeVries, T., & Weber, T. (2017). The export and fate of organic matter in the ocean: New constraints from combining satellite and oceanographic tracer observations. Global Biogeochemical Cycles, 31(3), 535-555.

Henson, S. A., Sanders, R., & Madsen, E. (2012). Global patterns in efficiency of particulate organic carbon export and transfer to the deep ocean. Global Biogeochemical Cycles, 26(1).

Mouw, Colleen B, Barnett, Audrey, McKinley, Galen A, Gloege, Lucas, Pilcher, Darren (2016). Global ocean flux rates. PANGAEA, https://doi.org/10.1594/PANGAEA.855594, In supplement to: Mouw, CB et al. (2016). Global ocean particulate organic carbon flux merged with satellite parameters. Earth System Science Data, 8(2), 531-541, https://doi.org/10.5194/essd-8-531-2016.

Weber, T., Cram, J. A., Leung, S. W., DeVries, T., & Deutsch, C. (2016). Deep ocean nutrients imply large latitudinal variation in particle transfer efficiency. Proceedings of the National Academy of Sciences, 113(31), 8606-8611.